Applied Thermal Engineering 180 (2020) 115752

Contents lists available at ScienceDirect

Applied Thermal Engineering

journal homepage: www.elsevier.com/locate/apthermeng

Development of a wind retrieval method for low-speed low-pressure flows for ExoMars

Álvaro Soria-Salinas[a,*], María-Paz Zorzano[b,a], Roberto Mantas-Nakhai[a], Javier Martín-Torres[a,c]

[a] Division of Space Technology, Department of Computer Science, Electrical and Space Engineering, Luleå University of Technology, 971 87 Luleå, Sweden
[b] Centro de Astrobiología (INTA-CSIC), Torrejón de Ardoz, 28850 Madrid, Spain
[c] Instituto Andaluz de Ciencias de la Tierra (CSIC-UGR), 18100 Granada, Spain

HIGHLIGHTS

- A novel wind speed retrieval is developed for Mars surface exploration.
- Retrieval method based on forced convection modelling on passive-cooling fins.
- Free flow speeds measuring capabilities demonstrated for pressures $P \geqslant 9.\ 9{\cdot}10^{-3}$ bar.
- Accuracy of ± 0.3 m/s for frontal winds at $U_\infty < 10$ m/s and lateral winds at $U_\infty < 6$ m/s.

ARTICLE INFO

Keywords:
Heat transfer coefficient
Forced convection
Wind tunnel
Nusselt number
Experiments
Mars

ABSTRACT

Forced convective heat transfer from three horizontally inclined rectangular-based cylinders (rods) has been studied experimentally under representative Martian near-surface air flows in the Aarhus Wind Tunnel Simulator (AWTS), Denmark. The testing campaign was developed for the HABIT (Habitability: Brines, Irradiation and Temperature) instrument, European payload on board the ExoMars 2022 Kazachok surface platform. The average heat transfer coefficient was determined from steady CO_2 flows at a pressure of 9.9 mbar, an ambient temperature of ~25 °C, and for horizontal free-stream velocities between 0.8 and 12 m/s. A retrieval algorithm to derive the wind speed from the average heat transfer coefficient estimated at each of the three HABIT Air Temperature Sensors (ATS) rods was calibrated within the AWTS. The ATS rods are placed one at the front of the instrument structure (ATS_2) and two on the sides (ATS_1 and ATS_3); and under Martian atmospheric conditions these rods serve as cooling fins. Several relationships between the Nusselt number and the Reynolds and Prandtl numbers reported in the literature were evaluated to model convective heat transfer from the ATS rods. Where needed, corrections to account for radiative heat transfer within the AWTS were implemented. The final retrieval method demonstrated that wind speed can be retrieved for frontal winds in the range of 0–10 m/s, with an error of ± 0.3 m/s, using the cooling profile of the ATS rod 3, and for lateral winds in the range of 0–6 m/s, with an error of ± 0.3 m/s, using the ATS rod 2 cooling profile.

1. Introduction

Many engineering applications require fluid flow velocity to be measured. The retrieval of low speeds is particularly interesting in a wide range of scenarios, such as the controlled flow in a cleanroom or the ventilation systems. The low velocities and the variable temperature typical of these applications usually requires flow sensors, capable of measuring convection at different ambient temperatures [5].

The characterization of the near-surface Martian winds has been a highly targeted objective by the scientific community since the very first missions to the surface of the planet. Understanding the role of wind is essential for a variety of scientific topics that concern the Martian dust dynamics, such as dust storms [6–8], dust accumulation [9–11], and the atmosphere thermal environment. Also, because wind has strong implications on engineering operations, such as the entry descent and landing stages of inter-planetary missions, it is critical for the general circulation models, which relay on in-situ wind measurements for the characterization of the planetary boundary layer [12–14].

The low-pressure and low temperature dusty gas flow on the surface of Mars still represents an engineering challenge for the surface

* Corresponding author.
E-mail address: alvaro.soria.salinas@gmail.com (Á. Soria-Salinas).

https://doi.org/10.1016/j.applthermaleng.2020.115752
Received 12 February 2020; Received in revised form 25 May 2020; Accepted 14 July 2020
Available online 22 July 2020
1359-4311/ © 2020 The Authors. Published by Elsevier Ltd. This is an open access article under the CC BY license (http://creativecommons.org/licenses/by/4.0/).

Nomenclature

a	Minor side length ATS rod cross-section, m
A1,A2	Minor side length HABIT CU structure, m
A_c	Cross-section area ATS rods, m^2
A_i	Area of surface i, m^2
A_s	Areal lateral surface ATS rod, m^2
b	Major side length ATS rod cross-section, m
Bi	Biot number
B1,B2	Major side length HABIT CU structure, m
C_P	Specific heat at constant pressure, J/(Kg K)
D_{CO_2}	Kinetic diameter of CO_2 molecule, m
dx	Differential rod element, m^3
dx_i	Surface i of dx, m^2
E_{bi}	Emitted power from black body surface i, W/m^2
F_{ij}	View factor leaving surface i and reaching surface j
G_i	Irradiation on surface i, W/m^2
h_c	Local convective heat transfer coefficient, W/(m^2·K)
h_{cxi}	Convective heat transfer coefficient at dx_i, W/(m^2·K)
$\overline{h}_c$	Average convective heat transfer coefficient, W/(m^2·K)
$\overline{h}_{cATSi}$	$\overline{h}_c$ for ATS rod i, W/(m^2·K)
	$\overline{h}_c$ from optimization using [1] approach, W/(m^2·K)
h_{Mopt}	$\overline{h}_c$ from optimization using [2] approach, W/(m^2·K)
h_{Popt}	$\overline{h}_c$ from optimization using [3] approach, W/(m^2·K)
h_{Fand}	$\overline{h}_c$ using V_{Tunnel} values for the [1] approach, W/(m^2·K)
$h_{McAdams}$	$\overline{h}_c$ using V_{Tunnel} values for the [2] approach, W/(m^2·K)
$h_{Perkins}$	$\overline{h}_c$ using V_{Tunnel} values for the [3] approach, W/(m^2·K)
h_r	Radiative heat transfer coefficient, W/(m^2·K)
$\overline{h}_r$	Average radiative heat transfer coefficient, W/(m^2·K)
$\overline{h}_s$	External radiative heat transfer coefficient, W/(m^2·K)
$\overline{h}_{sopt}$	Optimum $\overline{h}_s$, W/(m^2·K)
$\overline{h}_{sF}$	Optimum $\overline{h}_s$ using [1] approach, W/(m^2·K)
$\overline{h}_{sMc}$	Optimum $\overline{h}_s$ using [2] approach, W/(m^2·K)
$\overline{h}_{sP}$	Optimum $\overline{h}_s$ using [3] approach, W/(m^2·K)
$\overline{h}_{sW}$	Optimum $\overline{h}_s$ using [4] approach, W/(m^2·K)
$\overline{h}_{si}$	$\overline{h}_s$ for ATS i, W/(m^2·K)
$\overline{h}_{sri}$	$\overline{h}_s$ for ATS i from radiative model, W/(m^2·K)
h_T	Total heat transfer coefficient, $h_T = h_c + h_r$, W/(m^2·K)
$\overline{h}_T$	Average h_T, W/(m^2·K)
$h_{Whitaker}$	$\overline{h}_c$ using V_{Tunnel} values for the [4] approach, W/(m^2·K)
h_{Wopt}	$\overline{h}_c$ from optimization using [4] approach, W/(m^2·K)
J_i	Radiosity of surface i, W/m^2
k	Thermal conductivity, W/(m·K)
K_{ATS}	Thermal conductivity along ATS rod, W/(m·K)
K_{ATSi}	K_{ATS} for ATS rod i, W/(m^2·K)
k_B	Boltzmann constant, J/K
k_f	Fluid thermal conductivity, W/(m·K)
k_{f_0}	Fluid thermal conductivity at T = 273 K, W/(m·K)
k_n	Knudsen number
K_{opti}	Optimized thermal conductivity for ATS rod i, W/(m·K)
K_{optri}	K_{opti} optimized for $\overline{h}_{sri}$, W/(m·K)
L	Length ATS rod, m
L_c	Characteristic length, m
L_{cB}	Characteristic length, $L_{cB} = a{\cdot}b/[2{\cdot}(a+b)]$, m
$L_{c_{min}}$	Minimum characteristic length, m
m	m-parameter
$\overline{m}$	Average m-parameter
M	Mach number
Nu	Nusselt number
$Nu_{D_{90°}}$	Nusselt number for horizontal cylinder
Pr	Prandtl number
P	Pressure, Pa
$\dot{q}$	Net heat exchange through surface i, W/m^2
$\dot{q}_{cxi}$	Net convective heat flux per unit area at dx_i, W/m^2
$\dot{q}_l$	Circumferentially-averaged net radiative heat flux per unit length, W/m
$\dot{Q}_i$	Net radiative heat flux through ATS rod surface i, W
$\dot{Q}_{li}$	$\dot{Q}_i$ per unit length, W/m
$\dot{q}_{ext}$	External heat flux per unit length, W/m
$\dot{q}_{si}$	Net heat flux per unit area, W/m^2
R	CO_2 gas constant, J/(kg·K)
Re	Reynolds number
Re_{cr}	Critical Reynolds number
Re_A	Reynolds number based on A
Re_B	Reynolds number based on B
$S_{k_{CO_2}}$	Sutherland's constant for thermal conductivity, K
$S_{\mu_{CO_2}}$	Sutherland's constant for dynamic viscosity, K
St	Strouhal number
T	Temperature, K
T_a	Temperature at $\chi = 1$, K
T_b	Temperature at $\chi = 0$, K
T_{CU}	Temperature CU structure, K
T_f	Film temperature, $T_f = (T_\infty + T_s)/2$, K
T_{Ln}	Temperature at $\chi = 1/4$, K
T_{Probe}	Temperature measured within the AWTS, K
T_s	ATS rod average temperature, $T_s = (T_a + T_b + T_{Ln})/3$, K
T_{sxi}	Surface temperature at dx_i, K
T_{sx}	Local surface temperature, K
T_∞	Fluid temperature, K
U_∞	Free stream speed, m/s
$U_{x\infty}$	Free stream speed X-axis component, m/s
$U_{y\infty}$	Free stream speed Y-axis component, m/s
V_{Fand}	Free stream speed estimation using [1] approach, m/s
$\vec{V}_h$	Horizontal velocity vector, m/s
V_{Local}	Local wind speed estimated by the ATS, m/s
$V_{McAdams}$	Free stream speed estimation using [2] approach, m/s
$V_{Perkins}$	Free stream speed estimation using [3] approach, m/s
V_{Tunnel}	Free stream speed measured within the AWTS, m/s
$V_{Whitaker}$	Free stream speed estimation using [4] approach, m/s
x	x-coordinate along each ATS rod
X	X-axis for the CU reference system
Y	Y-axis for the CU reference system

Greek Symbols

α	Incidence angle, °
γ_i	Order of magnitude of optimum K_{opti}, W/(m·K)
γ_{ir}	Order of magnitude of radiative model $K_{opti}\|_r$, W/(m·K)
ε	Emissivity
ϵ	Absolute error in wind speed, $\|V_{Tunnel} - V_{Local}\|$, m/s
ϵ_{max}	Maximum absolute error in wind speed, m/s
ϵ_{min}	Minimum absolute error in wind speed, m/s
η_i	Order of magnitude of optimum $\overline{h}_{sopti}$, W/(m^2·K)
η_{ir}	Order of magnitude of radiative model $\overline{h}_{sri}$, W/(m^2·K)
θ	Excess temperature, $\theta = T - T_\infty$, K
θ_b	Excess temperature at $\chi = 0$, K
λ_f	Mean free-path, m
μ_f	Dynamic viscosity, N·s/m^2
μ_{f_0}	Dynamic viscosity at T = 273 K, N·s/m^2
σ	Stefan-Boltzmann constant, W/(m^2·K^4)
χ	Dimensionless distance along the ATS rods

missions when designing wind sensors. At the surface of Mars, pressures of $P \sim 700$ Pa and temperatures of $T \sim 240$ K, with daily temperature oscillations up to $\Delta T \sim 90$ K, are typically found. Several techniques have been explored to achieve a trade-off between robustness (which is critical for a landed mission), resolution, and power efficiency. Thermal anemometry is the preferred approach as it has proven successful on surface missions to date, where thermocouple sensors are widely used. These sensors are usually chosen because of their excellent behaviour in harsh environments [15]. In the context of Mars surface exploration, examples of thermal anemometry wind sensors are the NASA Viking landers 1 and 2 hot-film wind sensors [16–18], the NASA Mars Pathfinder hot wires [19,20], the NASA Mars Science Laboratory (MSL) Rover Environmental Monitoring Station (REMS) Wind Sensor (WS) [21–23], or the NASA Temperature and Wind Sensors for InSight (TWINS) instrument [24]. Furthermore, a similar concept was used in the design of the Mars Environmental Dynamics Analyzer (MEDA), one of the payloads of the NASA Mars 2020 rover [25].

The thermal anemometry approach has also been followed on the HabitAbility: Brines Irradiation and Temperature (HABIT) instrument, one of the two European payloads of the ExoMars 2022 Kazachok surface platform (SP), from Luleå University of Technology, Sweden. HABIT flight model (FM) is shown in Fig. 1-left, including the three air temperature sensors (ATS) of the instrument designed to provide the air temperature in the vicinity of the SP. These ATS consists of three thin rectangular-based rods, whereby the temperature is monitored along their axis at three points similarly to the REMS and TWINS ATS rods. Fig. 1-right shows a detail view of ATS_1.

In this work, we propose a novel wind speed retrieval technique developed for HABIT. The retrieval is based on the modelling of convective heat transfer around the HABIT ATS rods when immersed in a cross-flow. Thus, the retrieval uses the correlation between wind speeds and the averaged convective heat transfer coefficient around each rod. This correlation is performed through the modelled averaged Nusselt number (Nu) on each rod. The flow past cylindrical bodies is a typical configuration in multitude heat transfer applications, such as radiators and condensers heat exchangers, in chemical and food industry processes, or in the cooling of automotive parts or electronic components, and it has been extensively reported in literature under this configuration [26,27]. The robust design of the ATS makes them also potential candidates in applications where gas flow needs to be measured under extreme pressure and temperature conditions. For example, high temperature wells for drilling and exploration operations in the oil, gas and geothermal industries [28].

A wind tunnel campaign was conducted in the Aarhus Wind Tunnel Simulator (AWTS) [29] under representative near-surface Martian winds. The environmental values for the campaign were set according to REMS observations on board the Curiosity rover, on the surface of Mars. The HABIT engineering and qualification model (EQM), a replica of the flight model (FM) integrated in the SP, was tested during the campaign. The aim was to investigate the expected limitations and capabilities of the retrieval when applied to the EQM ATS rods, after integration on the SP, during operations on Mars. The calibration of the retrieval was performed for the expected range of wind speeds on the surface of Mars and, limited by the AWTS testing capabilities, at ambient temperature. The wind speed retrieval error was estimated by comparison with the wind tunnel wind speed reference values. The latter were computed through laser Doppler anemometry. Several existing averaged Nusselt number models reported in the literature were considered and analysed for forced convection modelling of the ATS rods. Finally, the expected errors of the final HABIT ATS wind retrieval were defined and presented for frontal and lateral winds. The retrieval developed in this research work is limited to horizontal winds.

2. Theoretical background

2.1. Fluid temperature retrieval: one-dimensional heat flux problem

The working principle of the ATS air temperature retrieval is based on the energy-balance law adapted from [30] to a rectangular-based fin exposed to open atmospheric conditions and with one end maintained at a constant elevated temperature. These fins correspond to the ATS rods attached to the HABIT Container Unit (CU), see Fig. 1-left. Here it is assumed that the CU structure to which each ATS rod is attached (1) has a high thermal inertia, compared to the rods; (2) presents a temperature difference with respect to ambient conditions; and (3) is thermally coupled with the full spacecraft. The CU and SP are expected to change their temperature smoothly over the day on Mars in response to: (1) solar radiation incidence; and (2) thermal coupling with the surface, surrounding air, and their own internal heating sources. The same sensing methodology continues in operation on the REMS

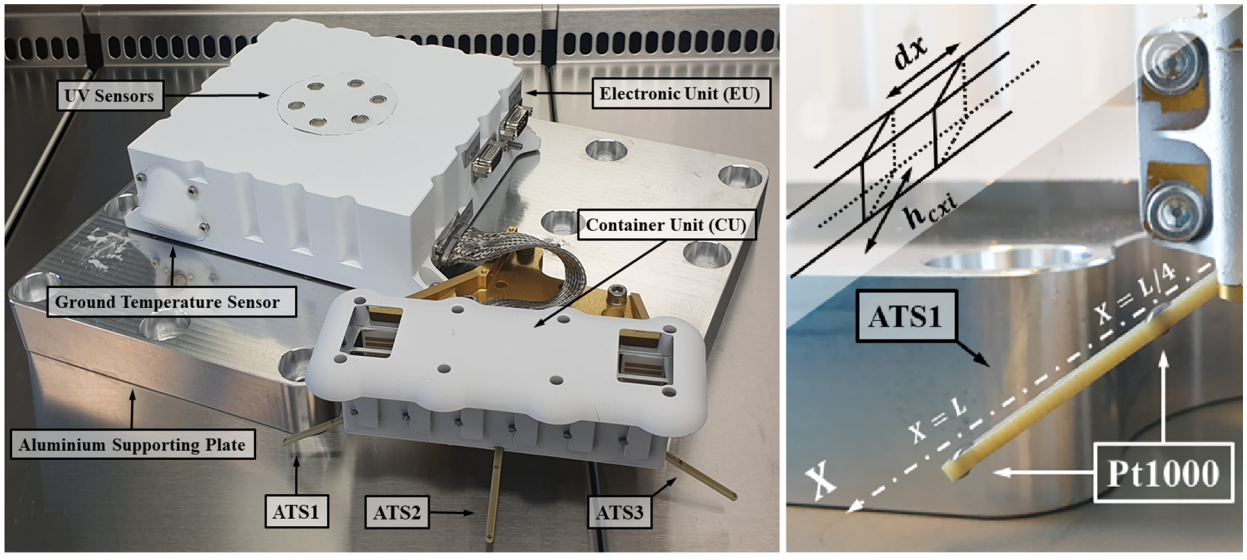

Fig. 1. (Left) HABIT flight model (FM) overall view with the three Air Temperature Sensors (ATS) pointing to the left-side (ATS_1), frontal side (ATS_2) and right side (ATS_3) of the Container Unit (CU). (Right) Detail view of the HABIT FM ATS_1 rod of length L. Three resistive temperature detectors (RTD) Pt1000 DIN EN 60751 class A are located at the tip, $x = L$, at $x = L/4$ and at $x = 0$ (not shown). The upper-left diagram represents a differential element of the rod, dx, and the convective heat transfer coefficients for the face dx_i of the differential element, h_{cxi}.

instrument since more than 7 years (at the time of this writing) on board the MSL Curiosity rover. Thus, the performance of this concept to monitor the air temperature in the vicinity of a landed spacecraft on Mars has been successfully demonstrated [22,23]. Considering the ATS rods long enough to assume one-dimensional heat conduction (i.e., assuming the Biot number, Bi, of each ATS rod to be Bi $\ll 1$) and steady-state conditions, we can express the energy balance equation at each differential element dx as:

$$\underbrace{\frac{d}{dx}\left(kA_c\frac{dT}{dx}\right)}_{\text{Conduction}} - \underbrace{h_c\frac{dA_s}{dx}(T-T_\infty)}_{\text{Convection}} - \underbrace{\varepsilon\sigma\frac{dA_s}{dx}\left(T^4-T_\infty^4\right)}_{\text{Radiation}} = 0, \tag{1}$$

where A_c and dA_s correspond respectively to the area of the cross-section, $A_c = a{\cdot}b = 6{\cdot}10^{-6}\text{m}^2$, and the differential area of the lateral surface, $dA_s = 2{\cdot}(a+b){\cdot}dx$, of each rod, respectively. The thermal conductivity k and emissivity ε are assumed constant in the rod. Note that here the local convective heat transfer coefficient, h_c, is the circumferentially averaged value of the four convective heat transfer coefficients derived from each lateral surface of a differential element dx of the ATS rod, h_{cxi} (see dx in Fig. 1-right). By definition, the latter would be $h_{cxi} = \dot{q}_{cxi}/[dx_i{\cdot}(T_\infty - T_{sxi})]$, where dx_i is the lateral surface i of the element dx, $\dot{q}_{cxi}$ would be the convective heat flux per unit area at the surface dx_i, and T_{sxi} would be the surface temperature at dx_i. As a result, $h_c(x) = \sum_{i=1}^{4} h_{cxi}/4$, which varies along the ATS rod as a function of x. Later in Section 3.2 it is demonstrated that Bi $\ll 1$, which means that it is reasonable to assume the temperature distribution at each differential element as uniform. This results in: (1) a uniform h_c across the rods' cross-sections; (2) a uniform temperature T in the differential element dx, which means that $T_{sxi} = \sum_{i=1}^{4} T_{sxi} = T_{sx}$ and $T_{sx}(x) = T(x)$; and (3) one-dimensional heat conduction along the rods. The heat losses at the rod tips are neglected.

By assuming a completely absorbing surrounding (i.e., a black body) at ambient temperature, it is possible to express the radiation terms as a function of a radiation coefficient, $h_r(x) = \varepsilon{\cdot}\sigma{\cdot}(T^2+T_\infty^2){\cdot}(T+T_\infty)$, at each position x, and then the total heat transfer coefficient in Eq. (1) as $h(x) = h_c + h_r$. All the properties of this system are evaluated at the film boundary layer, which is assumed to be at a film temperature $T_f = (T_s + T_\infty)/2$. Here, T_s is the average temperature of the ATS rod. Introducing the excess temperature, $\theta = (T - T_\infty)$, the m-parameter, $m = L{\cdot}\sqrt{(h{\cdot}A_s)/(k{\cdot}A_c)}$, and the dimensionless coordinate along the rods $\chi = x/L$, Eq. (1) can be rewritten:

$$\frac{d^2\theta}{d\chi^2} - m^2\theta = 0. \tag{2}$$

This non-linear two-point boundary value problem presents second derivatives in χ. Thus, two boundary conditions are required to provide a temperature distribution along the rods. If the temperature at the base of the rods, T_b, is known, it can be imposed that $\theta|_{\chi=0} = \theta_b$. Also, if the heat exchange at the tip of the rod with respect to the lateral surface is assumed negligible, $|\frac{d\theta}{d\chi}|_{\chi=1} \simeq 0$. Assuming the total heat transfer coefficient, $h(x)$, uniform at each rod cross-section, the temperature distribution along each rod can be expressed by Eq. (3):

$$\theta(\chi) = \theta_b\frac{cosh[\overline{m}(1-\chi)]}{cosh[\overline{m}]} \tag{3}$$

It should be noted that this solution for steady state conditions depends on the fluid temperature, T_∞, the temperature at the base of the rod, T_b, and average m-parameter, $\overline{m}$. The latter is a dimensionless number dependent on the geometry and thermal conductivity of the rods, which depends solely on the rod manufacturing, and the average total heat transfer coefficient, $\overline{h} = \overline{h}_c + \overline{h}_r$. In particular, for the ATS rods cross-section, $\overline{m}$ can be expressed as:

$$\overline{m} = L\sqrt{\frac{2{\cdot}(a+b){\cdot}\overline{h}}{k{\cdot}a{\cdot}b}}. \tag{4}$$

Each ATS rod includes three resistance temperature detectors (RTD) Pt1000 DIN EN 60751 class A, with an accuracy of $\pm$ 0. 15 K and a resolution of 0.05 K. These Pt1000 sensors measure temperatures at the ATS rods' base ($\chi = 0$), T_b, tip ($\chi = 1$), T_a, and at $\chi = 1/4$ from the base, T_{Ln}. Thus, Eq. (3) can be applied to the readings at $\chi = 0$ and $\chi = 1/4$ to obtain a system of two equations with two unknowns: T_∞ and $\overline{m}$. As implemented for the REMS ATS retrieval [22]:

$$T_a - T_\infty = \left(T_b - T_\infty\right){\cdot}\frac{1}{cosh[\overline{m}]} \tag{5}$$

$$T_{Ln} - T_\infty = \left(T_b - T_\infty\right){\cdot}\frac{cosh\left[\overline{m}{\cdot}\left(1-\frac{1}{4}\right)\right]}{cosh[\overline{m}]}. \tag{6}$$

Even though T_∞ and $\overline{m}$ are simultaneously obtained from the system (5)–(6) for every set of temperatures at each rod by the REMS ATS, only T_∞ is archived as a product at the Planetary Data System (PDS) [31–33]. $\overline{m}$ has been discarded so far. However, from Eq. (4) it can be inferred that the $\overline{m}$ values could provide useful information about the overall averaged heat transfer coefficient, and thus, about the wind speed. The averaged convective heat transfer coefficient values, affected by natural and forced convection, could be estimated as $\overline{h}_c = \overline{h}(\overline{m}) - \overline{h}_r(T_\infty, T_s)$ and correlated to horizontal wind speeds. Note that for each rod, $\overline{h}_r$ is computed with the average rod temperature $T_s = (T_a + T_{Ln} + T_b)/3$. Thus, this strategy has been developed and calibrated here to be implemented on the HABIT ATS temperature measurements in order to provide estimates of the surface wind-speeds during ExoMars mission operations at Oxia Planum, Mars.

2.2. Heat flux and forced convection modelling around the ATS rods

The HABIT wind retrieval is obtained by solving for the wind speed that corresponds to the averaged convective heat transfer coefficient derived from the estimated $\overline{m}$ values, $\overline{h}_c|_{\overline{m}}$. Thus, some modelling is required to correlate the derived $\overline{h}_c$ with the retrieved wind speed values. This is next addressed by modelling of the averaged Nusselt number for the ATS rods when immersed in a cross-flow.

2.2.1. Fluid flow regime

Before modelling forced convection, the expected flow regime on the surface of Mars must be known and modelled to assure that the hypotheses assumed in the retrieval are valid. The fluid flow around the rods was assumed to be an ideal and continuous CO_2 gas flow, with Knudsen number $k_n = \lambda_f/L_c < 0.1$ [34,35]. The characteristic length considered in this analysis is the diagonal of the rods cross-section, $L_c = 3.6{\cdot}10^{-3}$ m. The mean free path between CO_2 molecules is:

$$\lambda_f = \frac{k_B T}{\sqrt{2}\,\pi D_{CO_2}^2 P}. \tag{7}$$

The kinetic diameter considered was $D_{CO_2} = 3.94{\cdot}10^{-10}$ m according to [36]. The minimum scale to assume fluid-continuity under Mars surface conditions, as measured by REMS at Gale crater [37], is $L_{c_{min}} \sim 3.9 \cdot 10^{-5}$ m, much smaller than the length considered in the analysis, $L_{c_{min}}/L_c \sim 10^{-2}$. As a result, the fluid has been modelled in this study as an ideal continuous CO_2 gas. The transport parameters were also modelled according to the Mars near-surface pressure and temperature expected seasonal oscillations, between 700 and 1000 Pa and between 180 and 280 K, on average, respectively [37]. The temperature-dependent dynamic viscosity and conductivity of CO_2, $\mu_f(T)$ and $k_f(T)$, were modelled following the Sunderland's kinetic theory approach for a low-density CO_2 atmosphere. This theory is applicable for temperatures in the range of [190, 1700] K for $\mu_f(T)$ and [180, 700] K for $k_f(T)$, with an estimated error of $\pm$ 2% [38]:

Table 1
Average Nusselt number empirical approximations for horizontal cylinders provided by McAdams [2], Whitaker [4], Fand [1], and Perkins [3].

Author	*Re* range	Average Nusselt number expression
McAdams [2]	$[1, 10^5]$	$Nu = (0.4Re^{0.5} + 0.06Re^{2/3})Pr^{0.4}(\mu_f/\mu_s)^{0.25}$
Whitaker [4]	$[0.1, 10^3]$	$Nu = 0.32 + 0.43Re^{0.52}Pr^{1/3}$
Fand [1]	$[0.01, 2{\cdot}10^5]$	$Nu = 0.184 + 0.324Re^{0.5} + 0.291Re^{n}$ $n = 0.247 + 0.0407Re^{0.168}$
Perkins [3]	$[40, 10^5]$	$Nu = (0.31Re^{0.5} + 0.11Re^{0.67})Pr^{0.4}(\mu_s/\mu_f)^{0.25}$

$$\frac{\mu_f}{\mu_{f0}} \approx \left(\frac{T}{T_0}\right)^{3/2} \frac{T_0 + S_{\mu_{CO_2}}}{T + S_{\mu_{CO_2}}}, \tag{8}$$

$$\frac{k_f}{k_{f0}} \approx \left(\frac{T}{T_0}\right)^{3/2} \frac{T_0 + S_{k_{CO_2}}}{T + S_{k_{CO_2}}}, \tag{9}$$

where $\mu_{f0} = 1.370{\cdot}10^{-5}$ N · s/m^2 and $k_{f0} = 0.0146$ W/(m · K), and $S_{\mu_{CO_2}} = 222$ K and $S_{k_{CO_2}} = 1800$ K correspond to the CO_2 "Sutherland constants" (i.e., effective temperatures tabulated for each gas). The specific heat, $C_p\ (T)$, was modelled according to the following temperature-dependent polynomial expression for $P < 1$ bar and $T \in [200, 3500]$ K [36]:

$$\frac{C_p(T)}{R} = a_1 + a_2{\cdot}T + a_3{\cdot}T^2 + a_4{\cdot}T^3 + a_5{\cdot}T^4, \tag{10}$$

where $[a_1, a_2, a_3, a_4, a_5] = [3.85746029, 4.41437026{\cdot}10^{-3}$ K^{-1}, $-2.21481404{\cdot}10^{-6}$ K^{-2}, $2.45919022{\cdot}10^{-9}$ K^{-3}, $-1.43699548{\cdot}10^{-13}$ K$^{-4}]$. R is the CO_2 gas constant. The flow was assumed incompressible because the expected Mach number on Mars is $M \sim 10^{-3}$. Here, the nominal range of pressures and temperatures measured by REMS and applied to a CO_2 atmosphere were used as a reference.

Considering a horizontal gas flow normal to the ATS rods, the widest expected Re-range based on the cross-section diagonal, with Re $= \rho{\cdot}U_\infty{\cdot}L_c/\mu_f$ and $L_c \sim 3.6 \cdot 10^{-3}$ m, was 5< Re <120, although instant peak winds may not have been considered in the averaged values of this range [39]. Here, the horizontal projection of the rectangular cross-section of each rod has an aspect ratio AR ~1.2. No clear limit exists for the transition from laminar to turbulent flow around horizontal rectangular cylinders, where the AR of the cross section and the angle of incidence of the gas flow also conditions the critical Reynolds value, Re_{cr}. Experimental and numerical simulations have been performed for the flow region considered in this study for horizontal squared-based cylinders, where three regimes can be observed [40]. For AR = 1, a steady laminar flow is observed for Re $\lesssim$ 50, and an unsteady flow with a two-dimensional feature characterized by an alternative vortex shedding, called von Karman vortex street, is observed up to Re $\lesssim$ 194; a three-dimensional turbulent flow is observed for 190 $\lesssim$ Re $\lesssim$ 330. The average wind speeds observed on Mars by the REMS wind sensor (WS) were usually on the order of $v \lesssim 10$ m/s, an thus Re $\lesssim$ 38. Because an AR larger than 1 delays the transition between regimes from laminar to turbulent flow to higher Reynods values [41], the retrieval algorithm developed and tested in this study assumed an incompressible laminar flow.

2.2.2. Cross-flow Nusselt number modelling

The dependency with the Reynolds number and the Prandtl number, Pr $= C_P{\cdot}\mu_f/k_f$, of the heat transfer distribution on circular cylinders in cross-flow for different fluids is still poorly understood [42]. This process is usually correlated, for cylinders, by a power law relationship dependent on Re^{n_1} and Pr^{n_2} in terms of the averaged Nusselt number, Nu $= C{\cdot}(Re^{n_1} \cdot Pr^{n_2})$. The latter is defined as the ratio of convective to conductive heat transfer terms within a fluid domain, Nu $= \bar{h}_c{\cdot}L_c/k_f$. Thus, if the averaged Nusselt number is modelled as f(Re, Pr), the averaged convective heat transfer coefficient could be estimated as $\bar{h}_c|_{Nu} = (\mathrm{Re}, \mathrm{Pr}) \cdot k_f/L_c$. The later comparison of the coefficient $\bar{h}_c|_{Nu}$, that corresponds to the averaged Nusselt number model, with the coefficient $\bar{h}_c|_{\overline{m}}$, estimated from the average m-parameter, would then provide a non-linear equation that is solved for the free-stream speed U_∞ associated to the Re-value:

$$\bar{h}_c|_{Nu} = f(Re(U_\infty, T_\infty), Pr(T_\infty)){\cdot}k_f/L_c = \bar{h}_c|_{\overline{m}}, \tag{11}$$

The averaged Nusselt number modelling was performed by evaluating several existing models in literature for the expected regime of Re and Pr on the surface of Mars (as seen by REMS in [37]). Even though some previous studies investigated the Nusselt number distribution over squared-based cylinders [43], we found no relevant work for the Re and Pr flow regime considered. Therefore, the rectangular-based ATS rods were assumed as cylinders for the cross-flow average Nusselt number modelling. In particular, the empirical expressions for forced convection proposed by Fand [1], McAdams [2], Perkins [3], and Whitaker [4] were considered. These empirical models were developed for the expected range of Re and Pr on Mars. Their expressions have been collected in Table 1.

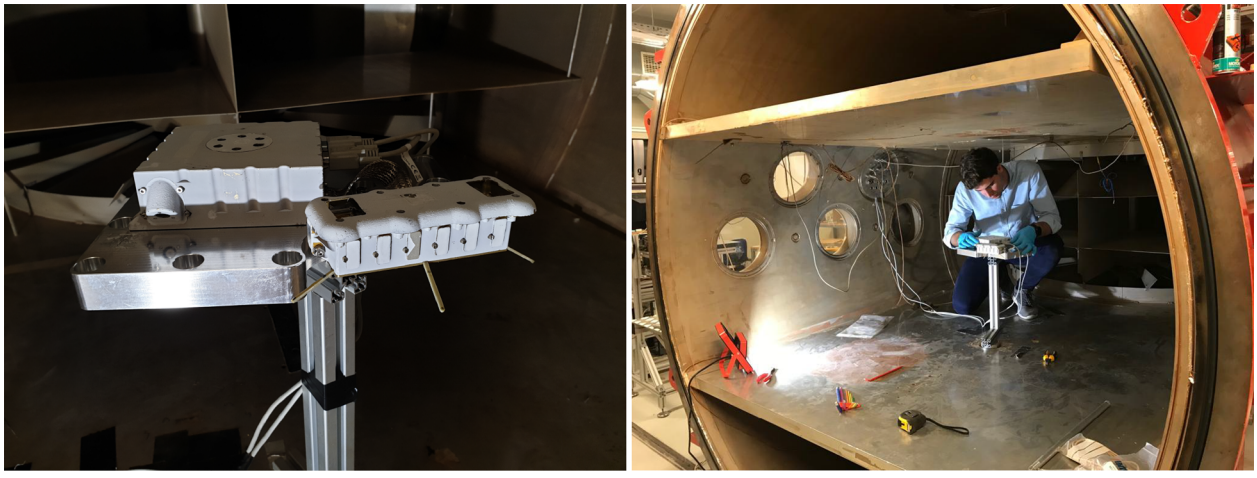

Fig. 2. (Left) HABIT EQM setup within the AWTS. The instrument is attached to an aluminium plate mimicking the attachment to the Kazachok surface platform. The aluminium plate was attached to a mast that could rotate in the horizontal plane. In the backside, the suctioning fan of the tunnel is visible. (Right) Cross-section of the wind tunnel during the installation of the HABIT EQM. The upper and lower horizontal aluminium plates that separate the testing area from the recirculating flow are visible. The tunnel windows and available flanges for the cabling connections can be seen on the walls of the tunnel.

3. Experimental validation in a Martian wind tunnel

Next we summarize the results of the tests performed with the HABIT EQM within the AWTS facility of the Aarhus University, Denmark.

3.1. Experimental setup: the AWTS facility

The AWTS facility consists of a low-pressure climate chamber designed with an internal recirculating system capable of reproducing low wind speeds of up to 20 m/s. The chamber is cylindrical, of about 8-m length and 2.5-m width, although the internal effective diameter for testing, free from wall disturbances, is ~ 0.4 m. The wind-generating system is powered by an electric motor Danfos VLT5001 that. This motor is located outside the vacuum chamber and moves an internal fan that is magnetically coupled. The tunnel presents an inner shell that can be depressurised to typical Martian surface pressure values (6–10 mbar). The shell is surrounded by an aluminium flange with a long copper coil pipe internally sealed that, for some configurations, can be used to inject liquid nitrogen and cool the wind tunnel. The gas within the chamber is evacuated through an Edwards single-stage rotatory pump. The pump allows to reach pressures of about 1 mbar in 1 h. The whole process is monitored with a Pfeiffer TPR265 pressure sensor. This pressure sensor operates optimally for only $P < 1$ mbar, which are lower than the typical operating pressures within the tunnel. The sensor is meant for air, presenting an error of 20% for pressure readings up to 100 mbar. For nominal configurations, the generated fluid flow presents a turbulence value of about 16% for wind speeds $U_\infty > 3$ m/s, which can be reduced to around 4% for most of the wind speeds in the range $U_\infty \in [0, 10]$ m/s when a double nylon mesh is installed at the beginning of the tunnel. This mesh generates, however, a pressure gradient in the fluid flow that reduces the correlation between the fan rotation frequency and the wind speed. This limits the maximum generated wind speeds to lower values, typically 8 m/s. As can be seen in Fig. 2, the gas flow circulates towards the location where the HABIT EQM is installed when suctioned by the fan that stands behind. The flow is then circulated back to the front of the tunnel through the channels that are above and below the two central horizontal panels.

The wind speed is controlled by modifying the revolutions per minute (RPM) of the fan from a control room. A typical relationship between RPM and wind speeds values of $U_\infty = \text{RPM}/60$ was used to preset the desired range of wind speeds during the wind campaign according to the AWTS technicians' instructions. After the tests, the actual wind speed values of the free flow of CO_2 in the wind tunnel was calibrated. This process was performed by using a set of fifteen predefined RPM values between 60 and 960 RPM of the fan, and the resulting axial wind speed values measured by a Dantec Laser Doppler Anemometer (LDA) system. The LDA was set to measure a single point located 0.5 m upstream, before reaching the testing setup. For each wind speed tested, the RPM and the LDA output values were averaged over 2 min. Fig. 3 shows the results of this process and the linear interpolation used to transform, for each HABIT test, RPM to wind-speed values.

The tests were performed at the AWTS under ambient temperature conditions. An artificial heating was applied to the instrument in order to generate the thermal gradients that are used to extract the m-parameter. On Mars, this gradient exists naturally due to the difference in temperatures between the huge landing platform and the thin Martian air. For these tests, however, we used the heating system of the HABIT Container Unit (CU). This system is designed to dehydrate the salts contained in the CU and thus, not meant to be used for this purpose. Test 1 was performed under CO_2 flows coming from $\alpha = -90°$ with respect to the CU frontal direction (X-axis, see Fig. 4), where the ATS rod 2 was exposed to unperturbed normal flows. Test 2 was performed under CO_2 flows coming from $\alpha = 0°$, where ATS rods 1 and 3 were exposed to ideal unperturbed normal flow conditions. The angle of incidence, α, was controlled, with resolution of 0.1°, by a rotating mast to which the EQM and aluminium plate were attached. The tests were performed at a pressure $P = 9.9$ mbar for RPM $\in [60, 720]$, which after calibration corresponded to $U_\infty \in [0.8, 11.1]$ m/s.

Each tested RPM value was set for 10 min and the data were later on averaged and converted to wind speed during post-processing activities. At $\alpha = 0°$ (Test 1), the front winds reached both ATS rod 1 and ATS rod 3 in the same conditions, since the CU is symmetric with respect to the X-axis. However, in Fig. 4 it can be observed that the experiment plate to which the CU is attached is not symmetric. This asymmetry represents a potential source of mismatch between the actual wind sensed at the locations of both rods. This implies that the subsonic fluid flow is not expected to surround both sensors in the same way because of different nearby obstacles. The actual distance of separation between the lateral ATS rods and the ExoMars SP is in fact comparable to the configuration of the ATS_3. This means that ATS_1 is placed, for this testing campaign, in an almost blind configuration as it is too close to the solid fixation plate. The reason of this setup is that, at the time of

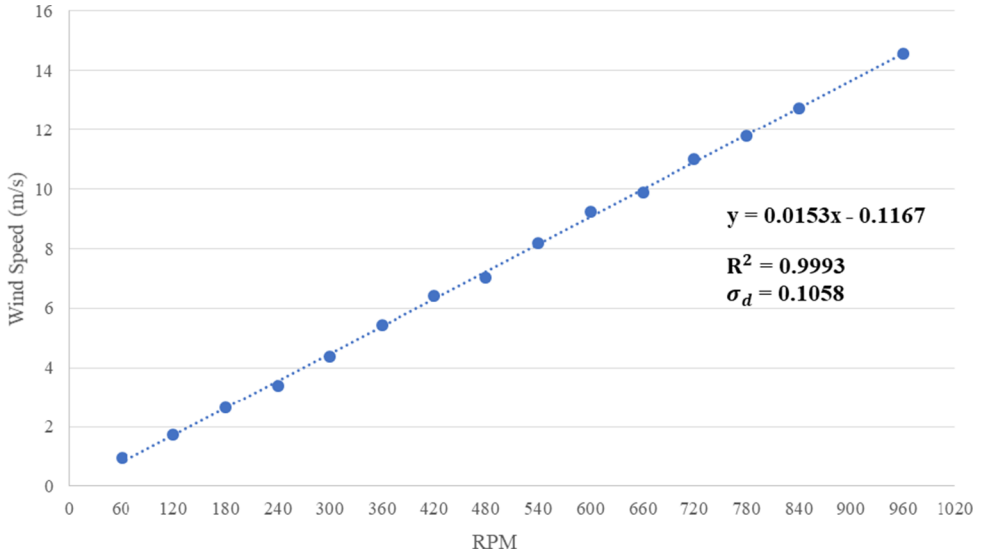

Fig. 3. Calibration of the AWTS wind speed. A linear interpolation has been implemented for the correlation between the wind tunnel fan RPM and the LDA wind speed values in the axial direction of the tunnel. The linear fit function, the R-squared value, and the standard deviation σ_d are also included.

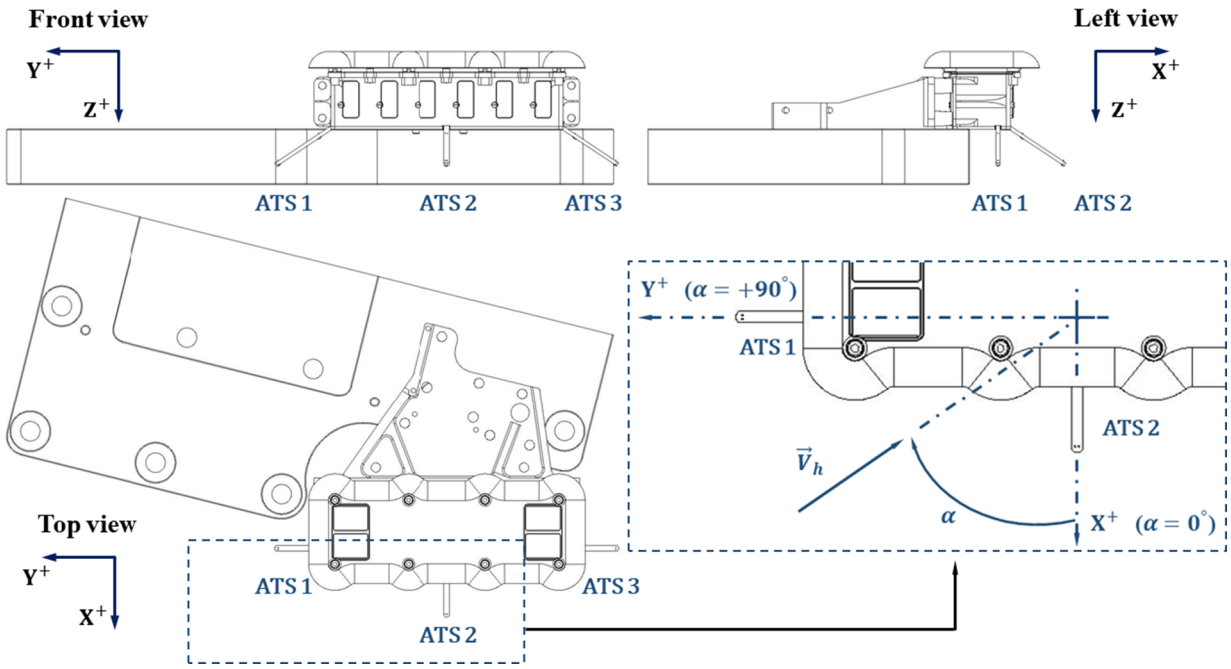

Fig. 4. Schematic views of the HABIT EQM setup for the AWTS tests. The reference system for the tests has been included in the top view, as well as the definition of the horizontal wind angle α for a horizontal wind vector V_h. For simplicity, the HABIT Electronic Unit (EU) has not been included in the drawings. A section of the aluminium plate used for the fixation of the instrument is included to show a more detailed view of the assembly.

the AWTS testing campaign, no other holding structure qualified for the HABIT EQM was available. Nevertheless, this asymmetry may be of interest in order to experience the interference placed by near-by objects on the wind flow and retrieval results.

Let us emphasize that the purpose of the ATS is to measure the air temperature and the wind speed locally, at the place where they are installed. This means that, although locally the speed may be lower because of the existence of obstacles close to the sensors, the free stream wind speeds to which the RPM reference values were correlated may be higher. It is therefore not possible to accurately use the nominal wind speed values provided by the tunnel for calibration and comparison of local wind speed measured by each ATS rod in all cases. Some deviation is expected depending on the local fluid flow and ATS rod considered. Furthermore, as mentioned above, the true configuration of the HABIT FM at the SP is slightly different from the setup showed in Fig. 4. The actual final relative angle between the FM CU and the SP, including the shape of the SP, are different: both ATS_1 and ATS_3 are expected to be equally close to the platform. In summary, although certain physical parameters such as thermal conductivity, physical dimensions, and emissivity, will be the same for the three ATS rods, they will be exposed to slightly different local wind fields and thus show different responses to the same incident wind during the campaign.

As a result, we shall first analyse the comparative response of the three ATS rods in the wind tunnel to a common wind field in order to understand how different the local response to a normal free flow is. Next, we shall consider the ATS rod whose response is the closest to the reference values as our reference sensor for calibration of the ATS true response. Then, those calibrated values shall be applied to the other sensors, which will provide now true local wind measurement estimates.

3.2. Measurement technique

The purpose of Test 1 and Test 2 was to demonstrate the correctness of the model by applying the wind retrieval to a full range of wind speeds under a predefined fixed orientation, normal to the ATS rods. This required the calibration of two elements of the described heat transfer problem: the ratio between the thermal conductivity and emissivity of the ATS rods in the axial direction, K_{ATSi}/ε, and the energy offset associated to the testing facility, unique to the setup described in Section 3.1. The latter is not expected on Mars. This offset is produced by: (1) the thermal interchange between the ATS rods and the overheated CU, which is heated continuously with a resistor at 60% of its maximal power (i.e. introducing 2.1 W locally at the CU) to generate the needed thermal profiles along the rods; and (2) the nearby metallic wind tunnel walls, the shelves that divide the tunnel, and the pole and aluminium plate where the HABIT instrument is attached to. These elements are also thermally coupled with the external laboratory ambient temperature. For the ratio K_{ATSi}/ε, on which the m-parameter depends, it was assumed, without loss of generality, an emissivity of $\varepsilon = 0.95$. This value is considered from the data-sheet of the Halogen Filled TG150 material the ATS rod glass-fibre laminates are made of. The thermal conductivity K_{ATSi} along the ATS rod i is expected to be a combination of the in-plane laminates' thermal properties and the internal wiring between Pt1000 sensors. In this study, the ATS rods have been assumed to be solid bodies with a uniform and constant thermal conductivity that accounts for this combination. For printed circuit boards (PCB) glass-fibre laminates, this value is typically of the order to ~ 0.8 W/(m·K) for the in-plane dimension [44].

The retrieval algorithm is based in the estimation of the wind speed value that makes equal the average convective heat transfer coefficient obtained through the modelling of the average Nusselt number at each rod, $\bar{h}_c|_{Nu}$, and the average convective heat transfer coefficient derived from the estimated average m-parameter, $\bar{h}_c|_{\bar{m}}$. From Eq. (11):

$$\bar{h}_c = \overbrace{\frac{\bar{m}^2 \cdot K_{ATS} \cdot a \cdot b}{L^2 \cdot 2 \cdot (a+b)} - \sigma\varepsilon\left(T_s^2 + T_\infty^2\right)\left(T_s + T_\infty\right)}^{\bar{h}_{cATSi}|_{\bar{m}} = \bar{h}_T|_{\bar{m}} - \bar{h}_r|_{ATSi}} = \overbrace{\frac{k_f}{L_c} \cdot Nu_{D_{90^\circ}}}^{\bar{h}_{cATSi}|_{Nu}}, \tag{12}$$

where $Nu_{D_{90^\circ}}$ represents the cross-flow averaged Nusselt number for horizontal cylinders when the fluid flow is normal to the rod lateral surface. We illustrate in Fig. 5-left an example (assuming $K_{ATS} = 0.5$ W/(m·K)) of the evolution of the ATS measured average convective heat transfer coefficient, $\bar{h}_c|_{\bar{m}} = \bar{h}(\bar{m}, K_{ATS}) - \bar{h}_r(T_\infty, T_s)$, and radiative heat transfer coefficient, $\bar{h}_r$. Similarly, and for the same thermal

conductivity, the theoretical convective heat transfer coefficient according to U_∞ measured by the tunnel is represented in Fig. 5-right, $\bar{h}_c|_{Nu}$. The curves are included for ATS rod 2 at $\alpha = -90°$ (Test 1), and for ATS_1 and ATS_3 at $\alpha = 0°$ (Test 2). Note that the $\bar{h}_c|_{Nu}$ curves naturally differ, for the same Nusselt number model, because of the different temperature profiles developed at each ATS rod, which are specific of the ATS rod and provide different values for the average ATS rod temperature T_s.

In Fig. 5-left it can be observed that $\bar{h}_c|_{Nu} \in [3, 16]$ W/(m^2· K) for the range $U_\infty \in [0.8, 12]$ m/s. The Biot number for the ATS rods during the testing campaign, Bi= $\bar{h}_c \cdot L_{cB}/K_{ATS}$, was then $0.004 < \text{Bi} < 0.02$, assuming $K_{ATS} = 0.5$. The characteristic length $L_{cB} = a \cdot b/[2 \cdot (a + b)]$ is the ratio of the ATS rod's volume to surface area, as usually defined for this calculation in solids [45]. Note that Bi $\ll 1$, which implies that it is reasonable to assume uniform temperatures across the ATS rod cross-sections in the heat exchange process during Test 1 and Test 2.

As can be observed when comparing the graphs in Fig. 5, at wind speeds $U_\infty \lesssim 4$ m/s, the convective heat transfer coefficient estimated from the m-parameter model gives a negative value that depends on the ATS rod. As pointed above, the reason for this offset is the presence of nearby local radiative heat sources that, at the low-pressure environment of the test ($P = 9.9$ mbar) and under the low wind speed values simulated, represent an important contribution to net heat-flux developed through the lateral surfaces of the ATS rods. To correct this offset from the setup, an additional average heat transfer coefficient term should be included in Eq. (12), $\bar{h}_s|_{ATSi}$, that accounts for the additional radiative heat sources from the surrounding surfaces. This correction was not included in the original m-parameter model because it was developed for operations under ambient open conditions. Eq. (12) is then rewritten and reads:

$$\overbrace{\frac{\overline{m}^2 \cdot K_{ATS} \cdot a \cdot b}{L^2 \cdot 2 \cdot (a+b)} - \sigma\varepsilon\left(T_s^2 + T_\infty^2\right)\left(T_s + T_\infty\right) - \frac{\dot{q}_{ext}}{2 \cdot (a+b)(T_s - T_\infty)}}^{\bar{h}_{cATSi}|_{\overline{m}} = \bar{h}_T|_{\overline{m}} - \bar{h}_r|_{ATSi} - \bar{h}_s|_{ATSi}} = \overbrace{\frac{k_f}{L_c} \cdot Nu_{D90°}}^{\bar{h}_{cATSi}|_{Nu}}, \tag{13}$$

where, according to dimensional analysis, $\bar{h}_s|_{ATSi}$ results from an external heat-flux per unit length, $\dot{q}_{ext}$, scaled with the rods' perimeter, $2 \cdot (a + b)$, and the temperature difference $(T_\infty - T_s)$.

The calibration of K_{ATSi} and h_{si} was performed by fitting the retrieved wind speeds from the ATS_2 temperature readings on Test 1, and from the readings of ATS_1 and ATS_3 on Test 2, to the reference free stream, U_∞, though a least-squared scheme. We assumed an emissivity for the ATS rods of 0.95, and let as free parameter K_{ATSi}, which can vary within the interval [0.3, 1.5] W/(m·K), and $\bar{h}_s|_{ATSi}$. The latter is inherent to the testing setup and, according to our radiative surface heat-exchange model estimates, could vary within $\bar{h}_s|_{ATSi} \in [5, 20]$ W/(m^2·K) (see Appendix A). Test 1 was performed for $U_\infty \in [0, 11]$, and Test 2 for $U_\infty \in [0, 12]$ m/s.

For the calibration of K_{ATSi}, only wind speeds lower than 6 m/s were considered. This means that the model is experimentally validated for the range 0 to 6 m/s. However, K_{ATSi} is a physical property and it can therefore be considered as calibrated for any other range of wind speed. We calculated the wind speed retrieval errors for the ranges of 0 to 10 m/s. The results may be extrapolated to higher wind regimes, but because of the tunnel limitations we could not demonstrate the actual error for $U_\infty > 12$ m/s.

4. Results and discussion

Fig. 6-left shows, for ATS rod 2 at $\alpha = -90°$, a comparison between (1) the convective heat transfer coefficient corresponding to the m-parameter, $\bar{h}_{cATSi}|_{\overline{m}}$, for each cross-flow Nusselt number model when introducing the optimized values for the thermal conductivity and radiative corrections, K_{opt} and $\bar{h}_{sopt}$; and (2) the theoretical convective heat transfer coefficient considering the same cross-flow Nusselt number models and optimal values but for the free stream wind speeds measured by the tunnel $V_{Tunnel} \equiv U_\infty$, $\bar{h}_{cATSi}|_{Nu}$. The temperatures measured by the tunnel probe, T_{Probe}, and the CU internal Pt1000 sensor, T_{CU}, are also shown. For $U_\infty \sim 4$ m/s, these temperatures clearly show the internal overheating of the tunnel because of, mainly, wall friction. Table 2 summarizes the absolute errors, $\epsilon = V_{Tunnel} - V_{Local}$, found when comparing the wind speed values locally retrieved by the ATS rod 2 with U_∞ for each Nusselt number model considered in this study.

Based on the CU horizontal plant dimensions, the obstacle is seen by the two-dimensional flow at $\alpha = -90°$ (Test 1) as a rectangle with an AR = B/A ~ 4. Here, A corresponds to the length of the small lateral faces of the CU in the X direction, where ATS_1 and ATS_3 are attached to, and B to the length of the front and rear faces in the Y dimension (see A1, A2, B1 and B2 in Fig. 7). The Reynolds number based on the shorter side of the CU, Re_A, is used according to the standard analysis performed over squared cylinders [41,46]. The analysis of the effect of the AR into Re_A and the Strouhal (St) number around rectangular cylinders has been extensively studied in the literature, both experimentally and numerically. For AR from 4 to 8, [46] found a complicated variation of the Re_A with the St and the base pressure. This was further investigated,

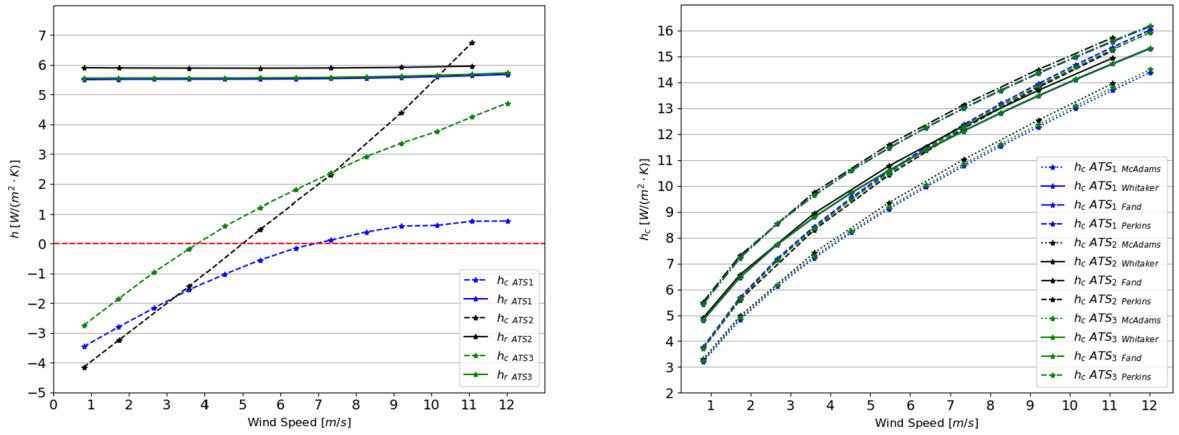

Fig. 5. (Left) Convective transfer coefficient measured by each ATS, estimated from the m-parameter, $\bar{h}_c|_{\overline{m}}$, and the equivalent heat transfer coefficient for the radiation losses, $\bar{h}_r$, at $\alpha = 0°$ for ATS_1 and ATS_3, and at $\alpha = -90°$ for ATS_2. The difference $\bar{h}_c = \bar{h}(\overline{m}, K_{ATS}) - \bar{h}_r(T_\infty, T_s)$ should provide the contribution of the convective heat transfer. (Right) Theoretical convective heat transfer coefficient predicted by each of the cross-flow Nusselt number models corresponding to the wind tunnel wind-speeds recorded at $\alpha = 0°$ for ATS_1 and ATS_3, and at $\alpha = -90°$ for ATS_2. The film temperature, T_f, and the average of the temperatures provided by the three thermistors at each ATSi, T_s, have been used for the evaluation of the transport coefficients.

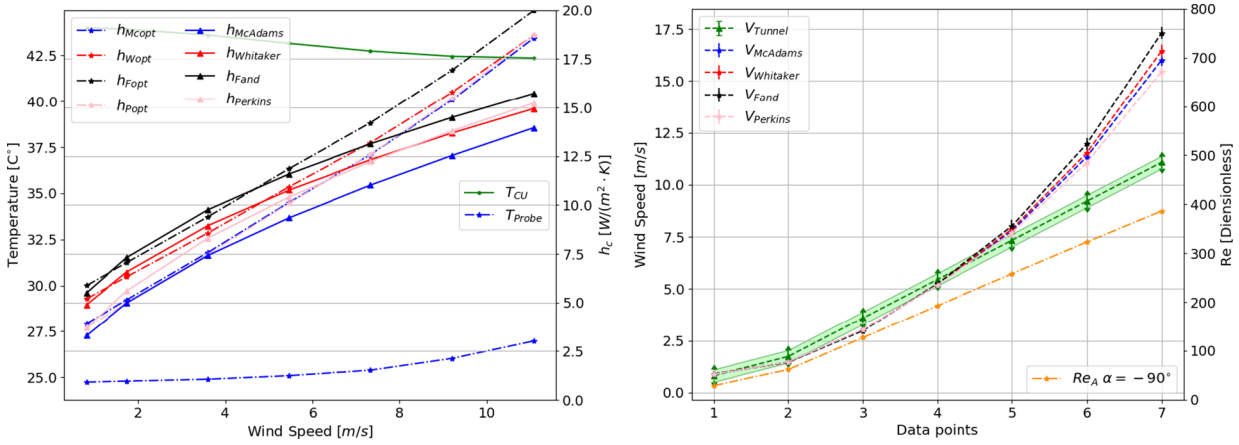

Fig. 6. (Left) HABIT EQM ATS$_2$ convective heat transfer coefficient $\overline{h}_{cATS_2}$ agreement at $\alpha = -90°$ for each Nusselt number model considered. Comparison between the $\overline{h}_{cATS_2}|_{\overline{m}}$ corresponding to the m-parameter obtained from the temperature readings when introducing the optimal values for K_{opt} and $\overline{h}_{sopt}$ of each cross-flow Nusselt number model (h_{Mopt}, h_{Wopt}, h_{Fopt}, h_{Popt} in the Figure), and the theoretical values of each $\overline{h}_c$ for the same cross-flow Nusselt number models assuming the tunnel wind speed values, $\overline{h}_{cATS_2}|_{Nu}$ ($h_{McAdams}$, $h_{Whitaker}$, h_{Fand}, $h_{Perkins}$ in the Figure). (Right) HABIT EQM ATS$_2$ wind speed agreement at $\alpha = -90°$ with respect to the wind tunnel measurements, $U_\infty \equiv V_{Tunnel}$, for each cross-flow Nusselt number model ($V_{McAdams}$, $V_{Whitaker}$, V_{Fand}, $V_{Perkins}$). The evolution of the Reynolds number based on the minor side of the CU, Re_A (see Fig. 4), is also included. The optimization was performed in the range of wind speeds $U_\infty \in [0, 6]$ m/s.

for a wider range of ratios ($0.6 \lesssim AR \lesssim 0.8$), numerically and for a wide range of Re_A by [46]. For rectangular sections with an AR >3, the separation of the laminar boundary layer in the leading edge is found to be for $Re_A \sim 90$ [46,47]. First, at these very-low Re_A-regimes, there is a steady reattachment right behind the leading edges. If Re keeps increasing, the flow finally separates at the trailing edges. At moderate Re_A-values, the initial separation at the leading edge is developed along the faces B1 and B2, reattaching alternatively for a brief period of time either to the front-B or the rear-B face during a period equivalent to a vortex shedding. In particular, for this aspect ratio, [46] observed that the separation bubbles are formed at both long faces (front and rear) for Re_A~200, and vortex shedding right after rear-A face. For higher Re_A-values, the separated flow tends again to reattach on the lateral surfaces at $Re_A \sim 500$, thanks to the aspect ratio of the obstacle [46]. However, in this case this reattachment is not steady, but alternative between front-B and rear-B faces. Similarly, the point of reattachment is not stationary, and it moves up and down downstream. Finally, for higher Reynolds numbers the transition from laminar to turbulent flow is produced. Although [41] did not study the critical Reynolds number for AR ~ 4, both AR ~ 2 and AR ~ 3 were tested. The former presented a $Re_{cr} \sim 500$, while the latter, a $Re_{cr} \sim 3{\cdot}10^3$. Thus, for AR ~ 4 the Re_{cr}-value is expected to be $Re_{cr} > 3{\cdot}10^3$.

For the first three values of wind speed on Fig. 6, $V_{Tunnel} < 3.6$ m/s, the retrieval perfectly follows the evolution of V_{Tunnel}, with a maximum error in average of 0.21 m/s. Re_A, was included in Fig. 6 for comparison. As a result, it can be observed that in this first sector $Re_A \lesssim 127$. This means that the horizontal laminar flow around the CU is apparently still attached to the lateral walls, or immediately steady-reattached after passing the leading edge, according to [41] (see first Re_A-range in Fig. 7). Because the ATS rod 2 is located at the middle of the larger side of the CU, it appears that this reattachment is produced before reaching the sensor. However, between the third and fourth tested points (i.e., $3.6 < V_{Tunnel} < 5.5$ m/s) the slope of the retrieved wind speed values changes, although the order of magnitude of the errors at $V_{Tunnel} = 5.5$ m/s is still similar to ±0.3 m/s of the wind tunnel speed values uncertainty (see Table 2 for the segment $V_{Tunnel} \in [0, 6]$ m/s). In this range of wind speeds, it appears that the reattachment point advanced in the Y^+ axis and finally reached the location of the ATS rod 2 (see second Re_A-range in Fig. 7). For $V_{Tunnel} > 5.5$ m/s, the separation bubbles could have developed along the entire front face of the CU as predicted. Here, $193 \lesssim Re_A \lesssim 386$ for $5.5 \lesssim V_{Tunnel} \lesssim 11$ m/s, and [46] estimated this point for $Re_A \sim 200$ (see third Re_A-range in Fig. 7). This phenomenon appears to be quantitatively reflected into the retrieved local speeds, which for this second segment of $V_{Tunnel} \in [6, 10]$ m/s leads to an average deviation with respect to the free flow wind speed of about ~2.4 m/s. As it can be observed, the Re_{cr} is not reached in this test, nor the regime of alternating reattachment of the boundary layer expected for $Re_A \sim 500$.

In Test 2, frontal winds ($\alpha = 0°$) reached the lateral ATS rods, namely both ATS$_1$ and ATS$_3$, perpendicularly and unperturbed. Because these rods are located at the lateral surfaces A1 and A2 (see Fig. 7) at just 5.55 mm distance from the CU front-B face, it is expected that the separation of the viscous boundary layer, in this case at $Re_B \sim 35$ for AR ~ 1/4, as well as the bubble formation and the final detachment that perturbed the flow around the ATS$_2$ rod in Test 1, does not affect the temperature probe of ATS$_1$ and ATS$_3$ rods for the range of wind

Table 2
Results from the optimization performed for $U_\infty < 6$ m/s over the ATS rod 2 temperature data at $\alpha = -90°$ (Test 1) for the thermal conductivity K_{ATS_2} and the average heat transfer coefficient $\overline{h}_{sATS_2}$. The minimum, maximum and average absolute error of each wind speed retrieval with respect to the reference (V_{Tunnel}), ϵ, have been included for comparison. The optimization was performed with respect to the theoretical convective heat transfer coefficients from each cross-flow Nusselt number model assumed, which are derived from the wind tunnel wind speed values, V_{Tunnel}.

N_u	ϵ for $V_{Tunnel} \in [0, 10]$ [m/s]			ϵ for $V_{Tunnel} \in [0, 6]$ [m/s]			ϵ for $V_{Tunnel} \in [6, 10]$ [m/s]		
–	ϵ_{min}	ϵ_{max}	ϵ_{ave}	ϵ_{min}	ϵ_{max}	ϵ_{ave}	ϵ_{min}	ϵ_{max}	ϵ_{ave}
				ATS 2, $\alpha = -90°$					
McAdams	0.1135	3.2642	0.8837	0.1135	0.2728	0.2025	1.2278	3.2642	2.2460
Whitaker	0.1370	3.4779	0.9468	0.1370	0.2964	0.2202	1.3225	3.4779	2.4002
Fand	0.1370	3.9531	1.0655	0.1370	0.3199	0.2378	1.4881	3.9531	2.7206
Perkins	0.1135	2.9553	0.8086	0.1135	0.2491	0.1907	1.1332	2.9553	2.0443

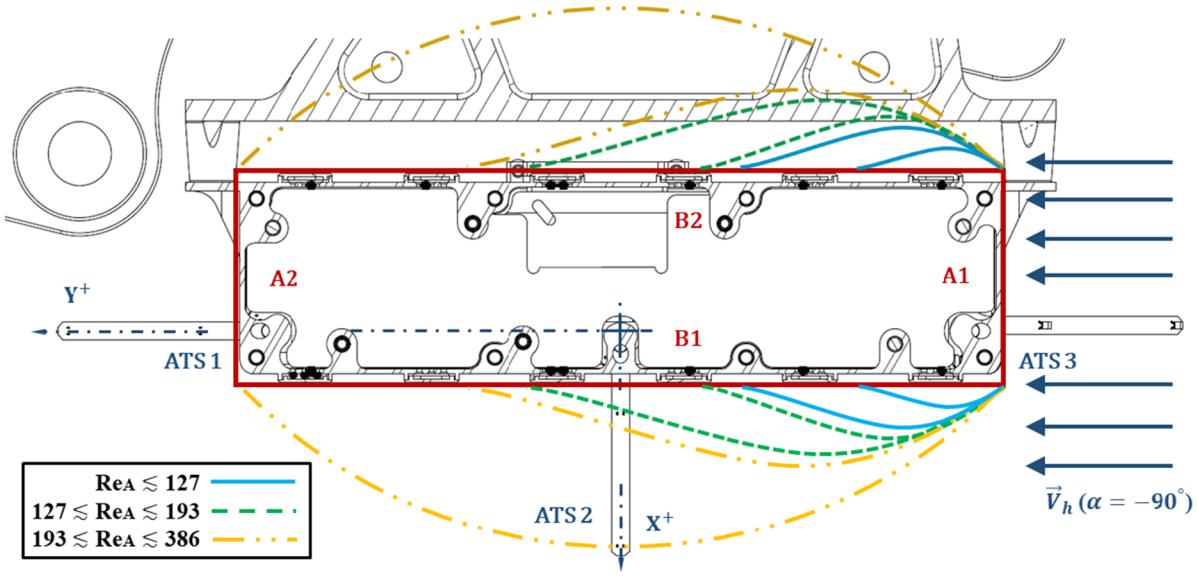

Fig. 7. Simplified rectangular geometry for the HABIT EQM CU structure when exposed to the horizontal two-dimensional CO_2 flow in Test 1 ($\alpha = -90°$). The aspect ratio of the simplified geometry is $A_i/B_i \sim 4$. A1, A2, B1 and B2 represent the front-A, rear-A, front-B and rear-B CU faces, respectively. The evolution of the reattachment of the CU viscous boundary layer has been qualitatively sketched for illustration considering three Re_A-regimes: $Re_A \lesssim 127$, $127 \lesssim Re_A \lesssim 193$ and $193 \lesssim Re_A \lesssim 386$.

speeds tested. The flow in this case is not expected to reattach to A1 and A2 since they are not long enough. However, in this situation the platform to which the HABIT CU is attached is located behind the rods. The platform will then interact or destroy the vortex shedding that developed after the trailing edge of the CU. Also, it should be kept in mind that, as mentioned above, ATS rod 1 is unfortunately too close to the experimental aluminium plate. This plate is an obstacle right after ATS_1 at a distance of the same order of magnitude of the rod length. Thus, some local fluid flow distortion is expected on ATS_1.

Fig. 8-left presents the comparison between $\overline{h}_{cATSi}|_{\overline{m}}$ and $\overline{h}_{cATSi}|_{N_u}$ for ATS_1 and ATS_3, as well as the wind tunnel internal gas flow overheating by wall friction and recirculation (see T_{Probe}, and T_{CU}). Fig. 8-right shows the corresponding wind speed predictions provided by the retrieval algorithm compared to the V_{Tunnel} values after calibration. Finally, Table 3 provides a quantitative summary of the agreement between wind speeds shown for both ATS_1 and ATS_3 in Test 2.

As can be observed in Fig. 3-left, $\overline{h}_{cATS1}|_{\overline{m}}$ shows a clear deviation beyond values of $V_{Tunnel} > 10$ m/s with respect to $\overline{h}_{cATS1}|_{N_u}$, which is later on reflected in the wind speeds. This deviation is experienced with independence of the cross-flow averaged Nusselt number selected for modelling forced convection around ATS_1 rod. ATS rod 3 shows, on the contrary, a good agreement for values $V_{Tunnel} \in [0, 12]$ m/s. Furthermore, a deviation from the theoretical predictions $\overline{h}_{cATS1}|_{\overline{m}}$ is observed for all models in ATS_1 for $V_{Tunnel} > 4$ m/s, although only the Perkins model shows a deviation larger than 0.5 W/(m²·K). Because ATS_1 and ATS_3 are exactly in the same relative position with respect to the wind field, the origin of this deviation must be in an external element not contemplated by either the radiative model corrections or the forced convection model. Nevertheless, the overall tendency of $\overline{h}_{cATS1}|_{\overline{m}}$ is similar to the $\overline{h}_{cATS1}|_{N_u}$, which was not observed for ATS rod 2 when $V_{Tunnel} > 6$ m/s. Even though the temperatures recorded by each ATS rod may be different, the evolution of the profiles should be similar or proportional with the increase of the wind speed values. A similar result is observed for the retrieved wind speeds for ATS_1 and ATS_3 in Fig. 8-right, and whose errors are collected on Table 3.

Although the linear fit from the calibration with the LDA offered a coefficient of determination $R^2 = 0.999$ (i.e., a standard deviation of $\sigma_d \sim 0.1$ m/s), an error of ±0.3 m/s was adopted for the wind tunnel

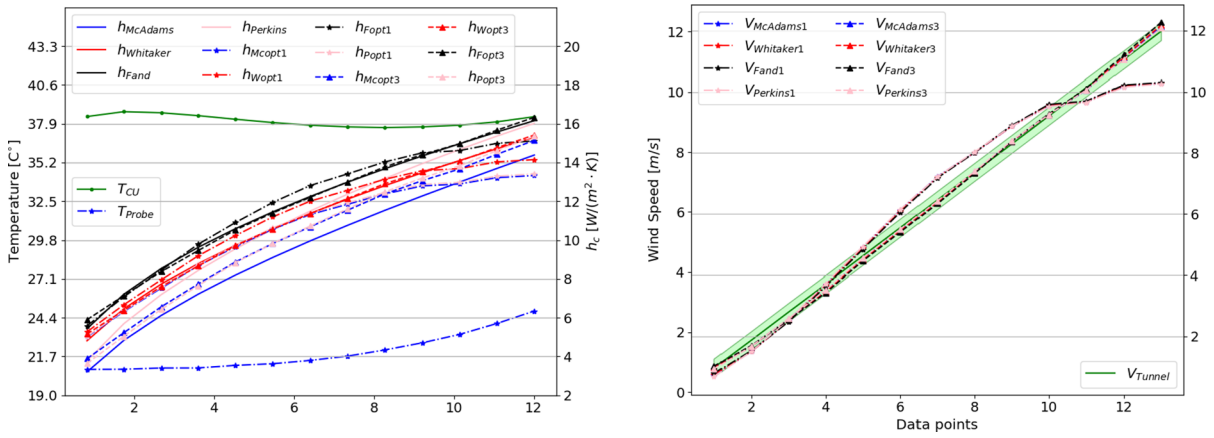

Fig. 8. (Left) HABIT EQM ATS_1 and ATS_3 $\overline{h}_{cATSi}|_{\overline{m}}$ and $\overline{h}_{cATSi}|_{N_u}$ agreement for frontal representative Martian winds ($\alpha = 0°$) at ambient temperature. Notation similar to Fig. 6-left, where the sub-index $i = 1, 3$ refers to ATS_1 and ATS_3 respectively. (Right) HABIT EQM ATS_1 and ATS_3 retrieval wind speed agreement for frontal representative Martian winds ($\alpha = 0°$) at ambient temperature. Notation similar to Fig. 6-right, where the sub-index $i = 1, 3$ refers to ATS_1 and ATS_3. Optimization performed for wind speeds $V_{Tunnel} \in [0, 6]$ m/s.

Table 3
Results from the optimization performed for $V_{Tunnel} < 12$ m/s over the ATS rod 1 and ATS rod 3 data at $\alpha = 0°$ (Test 2) for the thermal conductivity K and the average heat transfer coefficient $\bar{h}_s$. The minimum, maximum and average absolute error of each wind speed retrieval with respect to the reference (V_{Tunnel}), ϵ, have been included for comparison. The optimization is performed with respect to the theoretical convective heat transfer coefficients from each cross-flow Nusselt number model assumed, which are derived from the wind tunnel wind speed values.

Nu	ϵ for $V_{Tunnel} \in [0, 10]$ [m/s]			ϵ for $V_{Tunnel} \in [0, 6]$ [m/s]			ϵ for $V_{Tunnel} \in [6, 10]$ [m/s]		
–	ϵ_{min}	ϵ_{max}	ϵ_{ave}	ϵ_{min}	ϵ_{max}	ϵ_{ave}	ϵ_{min}	ϵ_{max}	ϵ_{ave}
				ATS 1, $\alpha = 0°$					
McAdams	0.0920	0.8328	0.4075	0.0920	0.6498	0.2666	0.3451	0.8328	0.4075
Whitaker	0.0696	0.8101	0.4008	0.0696	0.6271	0.2553	0.3679	0.8101	0.4635
Fand	0.0247	0.7874	0.3849	0.0247	0.5818	0.2252	0.3908	0.7874	0.3850
Perkins	0.1313	0.8328	0.4165	0.1313	0.6724	0.2816	0.3222	0.8327	0.4165
				ATS 3, $\alpha = 0°$					
McAdams	0.0021	0.1629	0.0665	0.0021	0.1629	0.0714	0.0155	0.1179	0.0592
Whitaker	0.0206	0.1629	0.0706	0.0206	0.1629	0.0820	0.0155	0.1179	0.0534
Fand	0.0012	0.2082	0.0936	0.0662	0.2082	0.1123	0.0012	0.1179	0.0655
Perkins	0.0190	0.1409	0.0673	0.0190	0.1176	0.0626	0.0301	0.1409	0.0743

speed according to the characterization of the AWTS viscous boundary layer performed by [29]. In Fig. 8-right, ATS rod 3 shows a fair agreement to the wind tunnel wind speeds tested, with a slight deviation towards the end of the test for $V_{Tunnel} > 10$ m/s still of the order of the 0.3 m/s margin. From Table 3, as happened for ATS rod 2, a more accurate retrieval for the first segment of wind speeds tested, $V_{Tunnel} \in [0, 6]$ m/s, can be observed for ATS rod 1 with respect to $V_{Tunnel} \in [6, 10]$ m/s. The averaged error value found in the former is $\lesssim$ 0. 28 m/s, similar to the $\sim$ 0. 21 m/s error found in average for ATS rod 2. For ATS_3 the first segment provides, in average, an error in wind speeds of $\lesssim$ 0. 11 m/s, and the second an error $\lesssim$ 0. 07m/s. The overall error for the range $V_{Tunnel} \in [0, 10]$ m/s is $\lesssim$ 0. 09 m/s, comparable to the standard deviation of the LDA $\sim$ 0.1 m/s.

Next, Table 4 summarizes the optimal values obtained from the optimization for the thermal conductivity and the heat transfer coefficient, K_{opt} and $\bar{h}_{sopt}$, for each of the Nusselt number models considered in this retrieval.

To accept the final values collected in Table 4, the $\bar{h}_{si}$ coefficients and the K_{opti} values should have the same order of magnitude than the $\bar{h}_{sri}$ predicted by the radiative heat exchange model summarized in Table 8 of the Appendix and K_{optri} (see Section 3.2), respectively. Furthermore, Table 8 also includes the order of magnitude of the optimum thermal conductivity K_{opti} for the values estimated through the radiative model $\bar{h}_{si}$ and for the wind speed range of each test.

For the case of ATS_3 in Table 4, the order of magnitude of the estimated $\bar{h}_{s3}$ for each Nusselt number model, η_3, is $\eta_3 \sim$ 5.2–7.5 W/(m²·K), similar to the $\bar{h}_{sr3}$ coefficients predicted by the radiative model, whose order is $\eta_{3r} \sim$ 7.2–7.6 W/(m²·K) (see Table 4). The order of magnitude of the optimal thermal conductivities K_{opt3} estimated in ATS_3, γ_3, on the other hand, is $\gamma_3 \sim$ 0.69–0.78 W/(m· K), similar to the optimized thermal conductivities K_{optr3} in the radiative model, $\gamma_{3r} \sim$ 0.6–0.69 W/(m·K). For ATS_2, and considering the optimization for $V_{Tunnel} \in [0, 6]$ m/s, $\eta_2 \sim$ 7.5–9.5 W/(m²·K), of the same order of $\eta_{2r} \sim$ 8.7–9.6 W/(m²·K). Also, the optimal thermal conductivities presented an order of magnitude $\gamma_2 \sim$ 0.61–0.69 W/(m·K), similar to $\gamma_{2r} \sim$ 0.46–0.67 W/(m·K). The results from the optimization were accepted because: (1) the values of the thermal conductivity were expected to be between 0.3, which is the thermal conductivity for the Halogen Filled TG150 glass-fibre laminates, and 0.8 W/(m·K), typical for in-plane PCB laminates' thermal conductivities; and (2) K_{opti} had a similar order of magnitude with respect to the optimized conductivity for $\bar{h}_{sri}$, K_{optri} in Table 8.

It should be noted that ATS_1 results showed $\eta_1 \sim$ 3.8–6.2 W/(m²·K), of the same order of $\eta_{1r} \sim$ 6.8–7-2 W/(m²·K). However, the optimum thermal conductivities presented $\gamma_1 \sim$ 1.11–1.26 W/(m·K), which is similar to $\gamma_{1r} \sim$ 0.91–1.06 W/(m·K) but around 0.3–0.4 W/(m·K) higher than the K_{opti} values for both ATS_2 and ATS_3. These values were also higher than the expected range of 0.3–0.8 W/(m·K). Changes of the order of 0.1–0.2 W/(m·K) could be expected because of possible differences between the attachment of the rods to the structure, manufacturing, connections and cable resistances, or limitations of the model. These results suggested that the wind speeds of the fluid flow when reaching ATS rod 1 were lower than the actual unperturbed wind speed set in the tunnel, U_∞. Because of the position of ATS rod 1, close to the aluminium plate, the horizontal subsonic velocity-field could be reduced in the surroundings of ATS_1 and thus be different to the unperturbed free stream that reaches ATS_3 at U_∞. The aluminium plate interference could be transmitted upstream to the ATS rod 1 boundary layer. The latter is observed in the value of $K_{opt1} \sim$ 0.95–1.1 W/(m·K), which is retrieved when the data are forced to fit the free-stream wind speeds U_∞.

4.1. Operational approach on Mars

The comparison of η_i with respect to η_{ir} for each cross-flow Nusselt number model on ATS_2 and ATS_3 (see Tables 4 and 8) suggested the

Table 4
Results from the optimization performed for the thermal conductivity K_{opt} and the average heat transfer coefficient $\bar{h}_{sopt}$ with respect to the theoretical convective heat transfer coefficients from each cross-flow Nusselt number model assumed, which are derived from the wind tunnel wind speed values. Optimization performed for ATS rod 2 at $\alpha = -90°$ (Test 1) and $V_{Tunnel} \in [0, 6]$ m/s, and for ATS_1 and ATS_3 at $\alpha = 0°$ (Test 2) and $V_{Tunnel} \in [0, 10]$ m/s. '*Mc*' refers to McAdams, '*W*' refers to Whitaker, '*F*' refers to Fand, and '*P*' refers to Perkins.

ATS	α	$\bar{h}_{s\ Mc}$	$\bar{h}_{s\ W}$	$\bar{h}_{s\ F}$	$\bar{h}_{s\ P}$	$K_{opt\ Mc}$	$K_{opt\ W}$	$K_{opt\ F}$	$K_{opt\ P}$
–	[°]	[W/(m²·K)]	[W/(m²·K)]	[W/(m²·K)]	[W/(m²·K)]	[W/(m·K)]	[W/(m·K)]	[W/(m·K)]	[W/(m·K)]
1	0.0°	3.8437	5.5825	6.2112	3.3925	1.2155	1.1106	1.1312	1.264
2	−90.0°	7.4736	8.9336	9.5184	7.2275	0.6713	0.6194	0.6464	0.6870
3	0.0°	5.2159	6.8544	7.5243	4.8026	0.7501	0.6847	0.6964	0.7806

Whitaker and Fand cross-flow Nusselt number approaches as the best options to be considered in the final wind speed retrieval. Both models showed differences in $K_{opti} \lesssim 0.06$ W/(m·K) between ATS rod 2 and 3, and differences $|K_{opti} - K_{optri}| \lesssim 0.05$ W/(m·K). These small differences are acceptable and may be possibly attributed to manufacturing or assembly biases. Finally, the error analysis performed on the test results demonstrated a better prediction of the Whitaker approach with respect to the Fand theory (see Tables 2 and 3) to evaluate $\bar{h}_{cATSi}|_{Nu}$. Thus, the former was chosen for the HABIT wind speed retrieval on Mars. As a result, the thermal conductivities will be assumed to be $K_{ATS2} = 0.62$ W/(m·K) and $K_{ATS3} = 0.69$ W/(m·K) on Eq. (13) for ATS_2 and ATS_3, respectively.

Results also suggested that the testing platform to which the HABIT EQM was attached interfered on the ATS_1 forced convection dynamics. ATS rod 1 was not exposed to an unperturbed horizontal velocity field at U_∞, but to a local fluid flow with a lower speed value. As a consequence, the latter was not correlated to the RPM set on the tunnel and calibrated through the LDA. Although the configuration of the EQM in this study was not identical to the final assembly on the ExoMars SP, the setup was useful to illustrate the role of nearby obstacles.

From the operational point of view, because the K_{opt1} values obtained for ATS rod 1 were found to be excessively high and both ATS_1 and ATS_3 present similar mechanical configurations, $K_{ATS1} \approx K_{ATS3} \pm 0.1$ W/(m·K) will be assumed on Mars for the retrieval of local wind speed in the vicinity of ATS rod 1. This in turn will lead to an error of $V_{1Local} \pm 0.93$ m/s for $U_\infty \in [0, 6]$ m/s. On the other hand, the results of these tests allowed for the estimation of the expected biases on the retrieval of frontal winds at U_∞ from the ATS rod 1 as a result of possible ExoMars SP interferences. However, for this test in the tunnel, the optimal thermal conductivity ($K_{opt1} = 1.11$ W/(m·K)) that minimizes this SP interference and allows for U_∞ retrievals with errors $\lesssim 0.81$ m/s can be used to compare with U_∞. These two modes are compared next in Fig. 9 to retrieve both V_{1Local} and U_∞. The Whitaker approach is applied on the three ATS rods, where ATS rod 2 was exposed to lateral winds and ATS rods 1 and 3 to front winds at $U_\infty \in [0, 10]$ m/s. It is worth mentioning that the retrieved ATS_1 local wind speed is lower than the free flow wind of the tunnel, confirming the role of the nearby plate interference discussed above. On the contrary, ATS_2 shows an increase in the local wind speed when the separation bubbles have developed along the entire front face of the CU as predicted, for wind speeds above 5.5 m/s.

As can be observed on Fig. 9, the wind speed retrieval will be capable of measuring frontal ($\alpha = 0°$) wind speeds at $U_\infty \pm 0.3$ m/s in the range of $U_\infty \in [0, 10]$ m/s (ATS_3), and lateral wind ($\alpha = \pm 90°$) speeds at $U_\infty = \pm 0.3$ m/s in the range of $U_\infty \in [0, 6]$ m/s (ATS_2). For any other orientation in the range of $\alpha \in [-90°, 90°]$, the ATS rods will measure the normal components of the horizontal free stream; that is, the horizontal wind vector may be able to be reconstructed by combining the retrievals of each ATS rod. For horizontal winds coming from the front-left quadrant (i.e., $\alpha \in [90°, 0°]$), the X^- component $U_{x\infty}$ will be measured by ATS_3 as $U_{x\infty} \pm 0.3$ m/s for $U_{x\infty} \in [0, 10]$ m/s, and the Y^+ component by ATS_2 as $U_{y\infty} \pm 0.3$ for $U_{y\infty} \in [0, 6]$ m/s. Similarly, for front-right horizontal winds (i.e., $\alpha \in [0°, 90°]$), X^- component will be measured as $U_{x\infty} \pm 0.81$ m/s for $U_\infty \in [0, 10]$ m/s by ATS_1 and Y^- components by ATS_2 as $U_{y\infty} \pm 0.3$ m/s for $U_{y\infty} \in [0, 6]$ m/s.

It has to be noted, though, that the flow around the ATS rods is conditioned by the platform the ATS rods are attached to. As it was shown for ATS rod 2, the development of the viscous boundary layer along the HABIT CU limited the retrieval of lateral winds to speeds $U_\infty < 6$ m/s. Thus, it is expected that for other wind directions a similar effect occurs, for all the three ATS sensors, limiting the applicability of the retrieval to a specific range of wind speed values that will depend on the specific direction of the fluid flow. The characterisation of this influence in the operability of the ATS sensors when retrieving the wind speed, particularly complex because of the instrument shape, would be one of the primary objectives in future wind tunnel campaigns. That

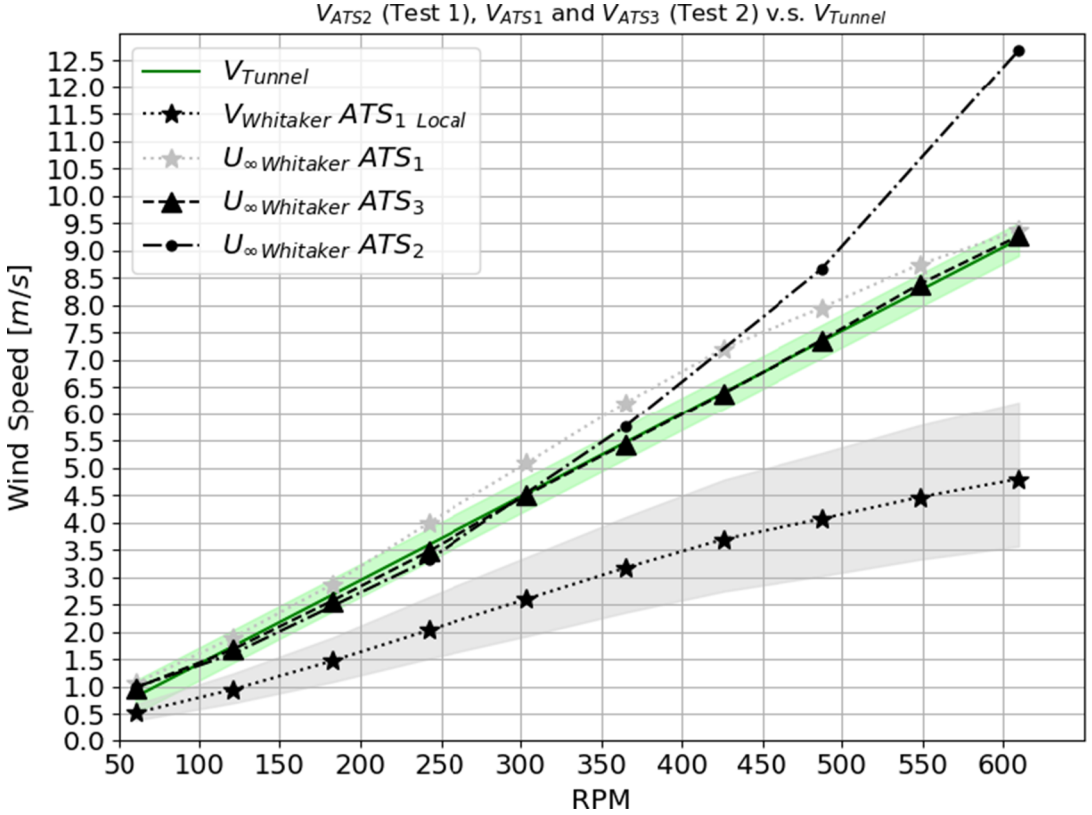

Fig. 9. HABIT wind speed retrieval algorithm output for front ($\alpha = 0°$) and lateral ($\alpha = \pm 90°$) horizontal wind fields, and for wind speeds $U_\infty \in [0, 10]$ m/s for different thermal conductivities.

said, the ATS sensor will provide the local wind speed, accurately, which may however differ from the free flow of the wind of Mars due to the interference with the Surface Platform.

5. Conclusions

The capabilities of wind speed retrieval algorithm for ExoMars have been experimentally assessed under representative near-surface Martian winds in the Aarhus Wind Tunnel Simulator. The retrieval is based on modelling forced convection around the three rectangular-based ATS rods of the HABIT instrument. With this method, the thermal profile of the fins can be used to retrieve the fluid temperature T_∞ and the local wind speed V_{local} simultaneously.

The EQM ATS rods thermal conductivity K_{ATS} was calibrated and the m-parameter model, designed to operate in open conditions, was adapted to operate within a low-pressure wind tunnel facility. The latter was performed by completing the m-parameter model with the effect of local radiative heat sources $\bar{h}_{si}$ that affect the ATS rods temperature condition. A least-square optimization of both K_{ATSi} and $\bar{h}_{si}$ was applied to each ATS rod in order to fit the theoretical average convective heat transfer coefficient, $\bar{h}_{cATSi}|_{Nu}$, derived from the AWTS wind speed data, to the estimated heat transfer coefficient from the m-parameter model, $\bar{h}_{cATSi}|_{\overline{m}}$. Two tests were performed at ambient temperature conditions ($T \sim 25°C$) and $P = 9.9$ mbar: Test 1, for lateral winds ($\alpha = -90°$) at $U_\infty \in [0, 10]$ m/s; and Test 2, for front winds ($\alpha = 0°$) at $U_\infty \in [0, 12]$ m/s. The results of the optimization were validated against a model of the expected radiative heat exchange between surfaces within the AWTS and applied to each ATS rod (see Appendix A). The optimization was accepted when (1) the order of magnitude of the radiative terms estimated from the radiative model $\bar{h}_{sri}$, and for the range of wind speed at each test, was similar to the optimized value for $\bar{h}_{si}$; (2) if the optimized thermal conductivity K_{opti} had a similar order of magnitude to the optimum conductivity value assuming $\bar{h}_{sri}$, $K_{optri}|_r$; and (3) if K_{opti} is of the same order of the expected values for a PCB based on Halogen Filled TG150 glass-fibre laminates.

The response of four experimental cross-flow average Nusselt number models for horizontal cylinders were assessed. The results demonstrated that the Whitaker model [4] is more adequate to predict the free stream speed. The wind retrieval was demonstrated to provide $U_\infty \pm 0.3$ m/s for frontal winds ($\alpha = 0°$) in the range of $U_\infty \in [0, 10]$ m/s, using ATS_3, and $U_\infty \pm 0.3$ m/s for lateral winds ($\alpha = \pm 90°$) in the range of $U_\infty \in [0, 6]$ m/s with ATS_2.

The wind-sensing retrieval capabilities were experimentally explored for steady flows for at least 10 min. The thermal equilibration time of the REMS ATS when measuring T_∞ (and thus $\overline{m}$) is reported to be 20 to 80 s [23]. Future studies will be devoted to investigating the actual response time of the ATS wind retrieval under varying wind conditions. Similarly, future wind campaigns will further explore the wind retrieval capabilities for horizontal winds in the range of $\alpha \in [-90°, 90°]$. The instrument was designed to measure the normal component of local winds and thus with the tests performed here the error in retrieval of the normal component has been calibrated. We conclude that for the operations on Mars, and due to the symmetric configuration of ATS_1 and ATS_3 with respect to the SP, we can use the ATS_1 to measure local winds by assuming $K_{ATS1} = K_{ATS3}$.

Declaration of Competing Interest

The authors declare that they have no known competing financial interests or personal relationships that could have appeared to influence the work reported in this paper.

Acknowledgements

The HABIT FM and EQM were manufactured by Omnisys Instruments AB, Sweden, in cooperation with the Luleå University of Technology (LTU). The HABIT project was funded by the Swedish National Space Agency (SNSA). We thank the ExoMars project team, European Space Agency (ESA), Roscosmos, Space Research Institute (IKI) and Omnisys Instruments AB for their hard work on the ExoMars 2022 mission. We acknowledge the Luleå University of Technology, the Wallenberg Foundation and the Kempe Foundation for support of the Mars research activities. ASS acknowledges the support of the LTU Graduate School of Space Technology. MPZ has been partially funded by the Spanish State Research Agency (AEI) Project No. MDM-2017-0737 Unidad de Excelencia "María de Maeztu"-Centro de Astrobiología (INTA-CSIC). We acknowledge the support of Mr. Jens Jacob Iversen and Dr. Jonathan P. Merrison from the Aarhus Wind Tunnel of the Aarhus University (Denmark).

Appendix A. Radiative model

To model the radiative heat exchange between the surfaces of the ATS rods and relevant surrounding surfaces, the geometry of the problem has been simplified to the coloured surfaces showed on Fig. 10. All the radiating surfaces were assumed to be separated by vacuum, a non-participating medium that does not emit, absorb or scatter radiation.

As can be observed in Fig. 10, ATS rod 1 and 3 are closer to the aluminium plate than ATS rod 2. However, while the external surfaces of the HABIT EQM are painted with space-grade white paint, similar to the paint used in REMS and with an emissivity $\varepsilon_{CU} = 0.88$, the aluminium plate presents a surface emissivity of the order of $\varepsilon_P = 0.05 - 0.09$. In addition to this, the temperature of this plate is also considerably lower than the temperature of the CU. The latter is heated by the CU heater set at 60% of its capacity, while the small heat flux introduced to the plate from the EU when the instrument is on, is negligible when comparing the huge thermal mass of the aluminium plate against the EU mass. As a result, together with the complex geometry of the lateral face of the aluminium plate mentioned earlier, the plate element was removed from the radiation exchange model. Furthermore, the instrument is expected to operate on Mars attached to another platform with different shape and surface emissivity. Thus, the inclusion of the aluminium plate into the model would artificially improve the retrieval prediction.

Considering grey, opaque and diffuse surfaces, the net heat power that leaves from or is absorbed by a specific surface of area A_i is, by definition:

$$\dot{q}_i = \frac{A_i \varepsilon_i}{1 - \varepsilon_i}\left[E_{bi} - J_i\right]. \tag{14}$$

It is possible to observe here that the heat transfer is driven by a potential $E_{bi} - J_i$ through a surface with a radiative surface resistance $(1 - \varepsilon_i)/(A_i \varepsilon_i)$. Considering an enclosure where the total irradiation reaching a surface A_i, G_i, is originated from the combination of the radiosities J_i of the rest of the n surfaces, it is possible to express the net heat power leaving from or absorbed by a surface A_i as a function of the view factors and the radiosities within the enclosure:

$$\dot{q}_i = A_i\left[J_i - \sum_{j=1}^{n} F_{ij} J_j\right] = \sum_{j=1}^{n} \frac{J_i - J_j}{\frac{1}{A_i F_{ij}}}. \tag{15}$$

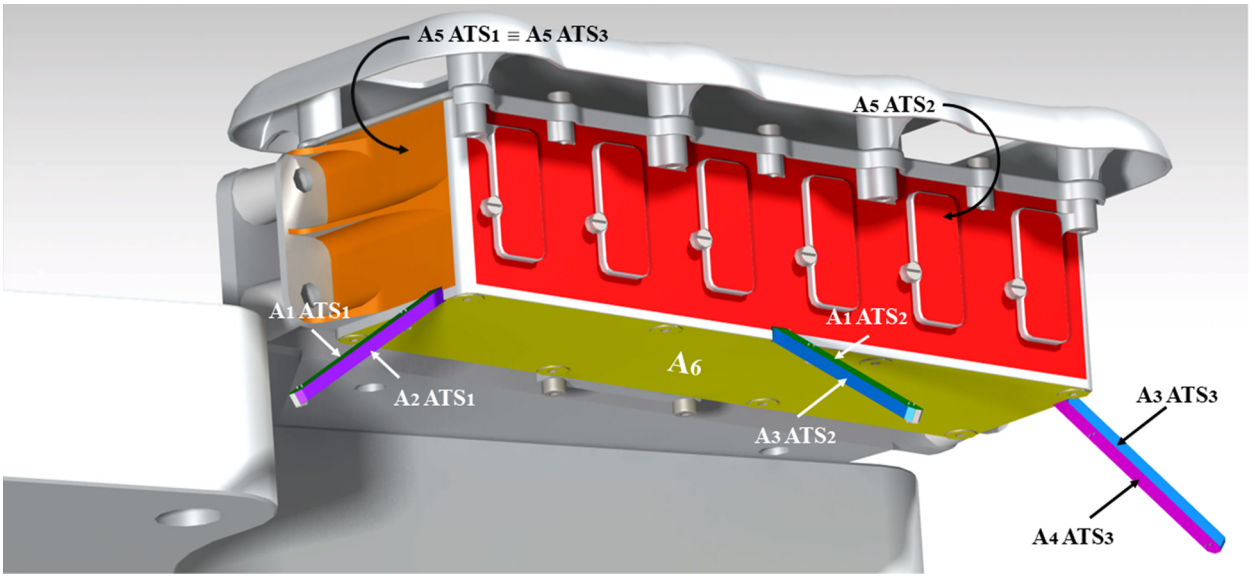

Fig. 10. Radiating surfaces considered for the heat exchange at the thermal radiation model. The view factors have been estimated by simplifying the geometry of the real surfaces A_1 to A_6 to rectangles of the same dimensions and area. The disposition and the value of the surfaces A_1 to A_4 are similar for each ATS rod, surface A_6 is also common to all the ATS rods, and surface A_5 is different for ATS rod 2 (red surface) with respect to the other two sensors (orange surface). For interpretation of the references to colour in this figure legend, the reader is referred to the web version of this article.

By combining Eqs. (14) and (15), it is possible to stablish an analogue to the radiative heat exchange between the relevant surfaces for each ATS rod. In this analogue, stationary conditions are considered, convection effects are neglected, and all surfaces are diffuse and grey. Fig. 11 shows the equivalent electrical circuit considered for this problem, and the Eqs. (16a)-(16f) shows the corresponding linear system to calculate the corresponding net radiative heat transfer rate from a surface $\dot{q}_i$, with $i = 1, 2, \ldots, 7$.

$$\frac{Eb_1 - J_1}{\frac{1-\varepsilon_1}{A_1\varepsilon_1}} + \frac{J_5 - J_1}{\frac{1}{A_1F_{15}}} + \frac{J_7 - J_1}{\frac{1}{A_1F_{17}}} = 0 \tag{16a}$$

$$\frac{Eb_2 - J_2}{\frac{1-\varepsilon_2}{A_2\varepsilon_2}} + \frac{J_5 - J_2}{\frac{1}{A_2F_{25}}} + \frac{J_6 - J_2}{\frac{1}{A_6F_{26}}} + \frac{J_7 - J_2}{\frac{1}{A_2F_{27}}} = 0 \tag{16b}$$

$$\frac{Eb_3 - J_3}{\frac{1-\varepsilon_3}{A_3\varepsilon_3}} + \frac{J_5 - J_3}{\frac{1}{A_3F_{35}}} + \frac{J_6 - J_3}{\frac{1}{A_6F_{36}}} + \frac{J_7 - J_3}{\frac{1}{A_3F_{37}}} = 0 \tag{16c}$$

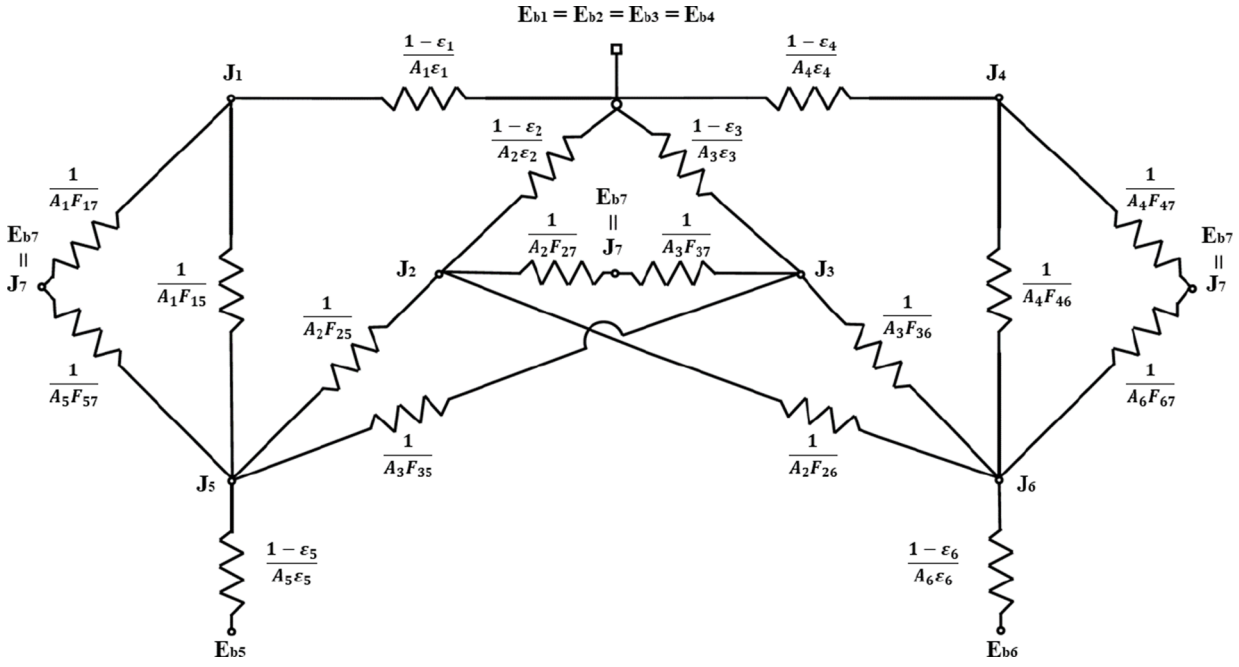

Fig. 11. Equivalent thermal circuit system for the heat exchange between each ATS surface and the CU within the AWTS.

Table 5
View factors F_{ij}, for $i = 1, ...,6$ and $j = 1, ...,7$, for ATS_1.

	ATS 1					
F_{ij}	$i = 1$	$i = 2$	$i = 3$	$i = 4$	$i = 5$	$i = 6$
$j = 1$	0.0000	0.0000	0.0000	0.0000	**0.0085**	0.0000
$j = 2$	0.0000	0.0000	0.0000	0.0000	**0.0053**	**0.0005**
$j = 3$	0.0000	0.0000	0.0000	0.0000	**0.0052**	**0.0007**
$j = 4$	0.0000	0.0000	0.0000	0.0000	0.0000	**0.0085**
$j = 5$	**0.0679**	**0.0118**	**0.0452**	0.0000	0.0000	0.0000
$j = 6$	0.0000	**0.0065**	**0.0272**	**0.0313**	0.0000	0.0000
$j = 7$	**0.9321**	**0.9817**	**0.9276**	**0.9687**	**0.9809**	**0.9909**

Table 6
View factors F_{ij}, for $i = 1, ...,6$ and $j = 1, ...,7$, for ATS_2.

	ATS 2					
F_{ij}	$i = 1$	$i = 2$	$i = 3$	$i = 4$	$i = 5$	$i = 6$
$j = 1$	0.0000	0.0000	0.0000	0.0000	**0.0032**	0.0000
$j = 2$	0.0000	0.0000	0.0000	0.0000	**0.0016**	**0.0008**
$j = 3$	0.0000	0.0000	0.0000	0.0000	**0.0016**	**0.0008**
$j = 4$	0.0000	0.0000	0.0000	0.0000	0.0000	**0.0010**
$j = 5$	**0.1072**	**0.0784**	**0.0784**	0.0000	0.0000	0.0000
$j = 6$	0.0000	**0.0451**	**0.0451**	**0.0384**	0.0000	0.0000
$j = 7$	**0.8928**	**0.8765**	**0.8765**	**0.9616**	**0.9912**	**0.9955**

$$\frac{Eb_4 - J_4}{\frac{4-\varepsilon_4}{A_4\varepsilon_4}} + \frac{J_6 - J_4}{\frac{1}{A_4F_{46}}} + \frac{J_7 - J_4}{\frac{1}{A_4F_{47}}} = 0 \tag{16d}$$

$$\frac{Eb_5 - J_5}{\frac{1-\varepsilon_5}{A_5\varepsilon_5}} + \frac{J_1 - J_5}{\frac{1}{A_1F_{15}}} + \frac{J_2 - J_5}{\frac{1}{A_2F_{25}}} + \frac{J_3 - J_5}{\frac{1}{A_3F_{35}}} + \frac{J_7 - J_5}{\frac{1}{A_5F_{57}}} = 0 \tag{16e}$$

$$\frac{Eb_6 - J_6}{\frac{1-\varepsilon_6}{A_6\varepsilon_6}} + \frac{J_1 - J_6}{\frac{1}{A_1F_{16}}} + \frac{J_2 - J_6}{\frac{1}{A_2F_{26}}} + \frac{J_3 - J_6}{\frac{1}{A_3F_{36}}} + \frac{J_7 - J_6}{\frac{1}{A_6F_{67}}} = 0 \tag{16f}$$

In Fig. 11, the node E_{b7} represents the inner walls of the tunnel, and was assumed that the room inside the facility is large enough to model the walls as a single black body. Consequently, the surface resistance for this node is assumed to be $(1 - \varepsilon_7)/(A_7 \cdot \varepsilon_7) \sim 0$, and thus $E_{b7} = J_7$. Only two emissivities were considered, where $\varepsilon_1 = \varepsilon_2 = \varepsilon_3 = \varepsilon_4 = \varepsilon_{ATS} = 0.95$ and $\varepsilon_5 = \varepsilon_6 = \varepsilon_{CU} = 0.88$. The temperature at each rod surface has been assumed similar and uniform, using the average of the three Pt1000 values at each rod: $T_{s1} = T_{s2} = T_{s3} = T_{s4} = (T_a + T_{Ln} + T_b)/3$. The surface temperature for the case of A_5 and A_6 were also assumed to be uniform and equal to the CU temperature, measured by an inner Pt1000 in contact with the CU structure, $T_{s5} = T_{s6} = T_{CU}$. The temperature considered for the tunnel inner walls was the tunnel's hanging fluid temperature probe, $T_{s7} = T_{Tunnel}$. Finally, only four areas are considered, since $A_1 = A_4$ and $A_2 = A_3$. The Nusselt unit sphere was used for the calculation of the view factors (see Eq. (17)), where the coloured areas, namely A_1 to A_6, were reduced to rectangles with the overall dimensions of each face. Tables 5–7 collect the calculated values of these view factors.

$$F_{12} = \frac{1}{A_1}\int_{A_1}\int_{A_2}\frac{cos\theta_1 cos\theta_2}{\pi l^2}\,dA_1\,dA_2. \tag{17}$$

With this radiative model it is possible to calculate, within the mentioned assumptions, a net radiative heat flux at each ATS rod surface, $\dot{Q}$ [W]. However, the goal of this model is to estimate the order of magnitude of the heat transfer coefficient corresponding to the external heat flux per unit length $\dot{q}_{ext}$ reaching the rod surfaces and that is scaled with the average temperature difference $T_s - T_\infty$ and the length $2\cdot(a + b)$, $\bar{h}_s|_{ATSi}$ (see Eq. (13)). Thus, first the net radiative heat flux at each ATS rod surface was scaled to a characteristic length to obtain $\dot{Q}_{li}$ [W/m], with $i = 1, ...,4$. The selected scale is the length of the ATS rods, common to all the four surfaces, $L = 0.036$ m. This scale agrees with the differential equation for the energy balance in temperatures (1). Thus, it is possible to define a differential lateral area dA_s that is later integrated along the rods between $x = 0$ and $x = L$

Table 7
View factors F_{ij}, for $i = 1, ...,6$ and $j = 1, ...,7$, for ATS_3.

	ATS 3					
F_{ij}	$i = 1$	$i = 2$	$i = 3$	$i = 4$	$i = 5$	$i = 6$
$j = 1$	0.0000	0.0000	0.0000	0.0000	**0.0085**	0.0000
$j = 2$	0.0000	0.0000	0.0000	0.0000	**0.0052**	**0.0007**
$j = 3$	0.0000	0.0000	0.0000	0.0000	**0.0053**	**0.0005**
$j = 4$	0.0000	0.0000	0.0000	0.0000	0.0000	**0.0085**
$j = 5$	**0.0679**	**0.0452**	**0.0118**	0.0000	0.0000	0.0000
$j = 6$	0.0000	**0.0272**	**0.0065**	**0.0313**	0.0000	0.0000
$j = 7$	**0.9321**	**0.9276**	**0.9817**	**0.9687**	**0.9809**	**0.9909**

Table 8
Averaged heat transfer coefficient $\bar{h}_{sr}$ and optimised K_{optr} estimated from the radiative heat exchange model for ATS_2 at $\alpha = -90°$, and for ATS_1 and ATS_3 at $\alpha = 0°$. "Mc" refers to McAdams, "W" refers to Whitaker, "F" refers to Fand, and "P" refers to Perkins.

ATS	α	$\bar{h}_{s\ min}$	$\bar{h}_{s\ max}$	$\bar{h}_{s\ AVE}$	$K_{opt\ Mc}$	$K_{opt\ W}$	$K_{opt\ F}$	$K_{opt\ P}$
–	[°]	[W/(m²·K)]	[W/(m²·K)]	[W/(m²·K)]	[W/(m·K)]	[W/(m·K)]	[W/(m·K)]	[W/(m·K)]
1	0.0	6.7963	7.2697	7.0478	0.9163	0.9749	1.0547	0.9226
2	−90.0	8.7408	10.8233	9.6523	0.4206	0.4576	0.5079	0.4240
2*	−90.0	8.7408	9.5859	9.1395	0.4750	0.58017	0.6702	0.4642
3	0.0	7.2352	8.0780	7.5853	0.5976	0.6357	0.6873	0.6018

to obtain the overall heat flux per unit surface in the rod. This integration is one-dimensional, as it does not distinguish faces at the ATS rod. As a result, we considered $\dot{q}_l = \sum_{i=1}^{4} \dot{Q}_{li}/4$ [W/m] as the circumferentially-averaged net radiative heat flux per unit length. At this point, the average heat transfer coefficient that collects the effect of the external radiative heat flux reaching the ATS rod i was the sum of the radiative losses coefficient $\bar{h}_r|_{ATSi}$ to the net coefficient:

$$\bar{h}_s|_{ATSi} = \left| \frac{\dot{q}_l}{2{\cdot}(a+b)(T_{si} - T_\infty)} \right| + |\bar{h}_r(\varepsilon)|_{ATSi}|,\ i = 1,\ \ldots, 3. \tag{18}$$

Note in Eq. (18) that $\dot{q}_l \neq \dot{q}_{ext}$. The former is referred to the net heat flux per unit length while the latter is referred to the incident heat flux per unit length. The net heat flux per unit area $\dot{q}_{si}$ [W/m²] at each lateral face of the ATS rod i can also be calculated directly from the $\dot{Q}_i$. The application of the radiative model to the temperature profiles collected in Test 1 from ATS rod 2 and Test 2 from ATS rod 1 and 3 provided the evolution of the radiative terms $\bar{h}_{sri}$. These were later introduced in the wind retrieval algorithm to estimate the corresponding optimum thermal conductivity according to each cross-flow Nusselt number approach, K_{optr}. The results of this analysis are collected in Table 8.

References

[1] R.M. Fand, K.K. Keswani, A continuous correlation equation for heat transfer from cylinders to air in crossflow for reynolds numbers from 10^{-2} to 2×10^5, Int. J. Heat Mass Transf. 15 (3) (1972) 559–572.
[2] W.H. McAdams, Heat Transmission, 3rd ed., McGraw-Hill, New York, 1954.
[3] H.C. Perkins, J.G. Leppert, Local heat-transfer coefficients on a uniformly heated cylinder, Int. J. Heat Mass Transf. 7 (2) (1964) 143–158.
[4] B.G. Van Der Hegge Zijnen, Modified correlation formulae for the heat transfers by natural and by forced convection from horizontal cylinders, Appl. Sci. Res. 6 (2–3) (1956) 129–140.
[5] M.S. Ashhab, A. Al-Salaymeh, Optimization of hot-wire thermal flow sensor based on a neural net model, Appl. Therm. Eng. 26 (8) (2006) 948–955.
[6] C.E. Newman, S.R. Lewis, P.L. Read, F. Forget, Modeling the Martian dust cycle 1. Representations of dust transport processes, J. Geophys. Res. 107 (E12) (2002) 5123.
[7] M.A. Kahre, J.R. Murphy, R.M. Haberle, Modeling the Martian dust cycle and surface dust reservoirs with the NASA Ames general circulation model, J. Geophys. Res. 111 (E06008) (2006).
[8] S. Basu, M.I. Richardson, Simulation of the Martian dust cycle with the GFDL Mars GCM, J. Geophys. Res. 109 (E11006) (2004).
[9] J.-B. Madeleine, F. Forget, E. Millour, L. Montabone, M.J. Wolff, Revisiting the radiative impact of dust on Mars usingthe LMD Global Climate Model, J. Geophys. Res. 116 (E11010) (2011).
[10] D.M. Hassler, C. Zeitlin, R.F. Wimmer-Schweingruber, B. Ehresmann, S.R.C. Rafkin, J.L. Eigenbrode, D.E. Brinza, et al., Mars' surface radiation environment measured with the Mars Science Laboratory's Curiosity Rover, Science 343 (6169) (2014) 1244797.
[11] A. Vicente-Retortillo, F. Valero, L. Vázquez, G.M. Martínez, A model to calculate solar radiation fluxes on the Martian surface, J. Space Weather Space Clim. 5 (A33) (2015).
[12] J. Pla-Garcia, S.R.C. Rafkin, M.A. Kahre, J. Gomez-Elvira, V.E. Hamilton, S. Navarro, J. Torres, et al., The meteorology of Gale crater as determined from rover environmental monitoring station observations and numerical modeling. Part I: Comparison of model simulations with observations, Icarus 280 (2016) 103–113.
[13] S.C.R. Rafkin, J. Pla-Garcia, M.A. Kahre, J. Gomez-Elvira, V.E. Hamilton, M. Marín, S. Navarro, et al., The meteorology of Gale Crater as determined from Rover Environmental Monitoring Station observations and numerical modeling. Part II: Interpretation, Icarus 280 (2016) 114–138.
[14] C.E. Newman, J. Gómez-Elvira, M. Marin, S. Navarro, J. Torres, M.I. Richardson, J.M. Battalio, et al., Winds measured by the Rover Environmental Monitoring Station (REMS) during the Mars Science Laboratory (MSL) rover's Bagnold Dunes Campaign and comparison with numerical modeling using MarsWRF, Icarus 291 (2017) 203–231.
[15] Y. Li, Z. Zhang, C. Zhao, X. Hao, N. Dong, W. Yin, Z. Pang, Laser based method for dynamic calibration of thermocouples, Appl. Therm. Eng. 174 (2020) 115276.
[16] K.L. Jones, R.E. Arvidson, E.A. Guinness, S.L. Bragg, S.D. Wall, C.E. Carlston, D.G. Pidek, One Mars Year: viking lander imaging observations, Science 204 (4395) (1979) 799–806.
[17] S.L. Hess, R.M. Henry, C.B. Leovy, J.A. Ryan, J.E. Tillman, Meteorological results from the surface of Mars: Viking 1 and 2, J. Geophys. Res. 82 (28) (1977).
[18] T.E. Chamberlain, H.L. Cole, R.G. Dutton, G.C. Greene, J.E. Tillman, atmospheric measurements on Mars: the Viking Meteorology Experiment, Bull. Am. Meteorol. Soc. 57 (9) (1976) 1094–1105.
[19] J.T. Schofield, J.R. Barnes, D. Crisp, R.M. Haberle, S. Larsen, J.A. Magalhães, J.R. Murphy, et al., The Mars Pathfinder Atmospheric Structure Investigation/ Meteorology (ASI/MET) Experiment, Science 278 (5344) (1997) 1752–1758.
[20] R. Sullivan, R. Greeley, M. Kraft, G. Wilson, M. Golombek, K. Herkenhoff, J. Murphy, et al., Results of the Imager for Mars Pathfinder windsock experiment, J. Geophys. Res. 105 (E10) (2000) 24547–24562.
[21] M. Domínguez, V. Jiménez, J. Ricart, L. Kowalski, J. Torres, S. Navarro, J. Romeral, L. Castañer, A hot film anemometer for the Martian atmosphere, Planet. Space Sci. 56 (8) (2008) 1169–1179.
[22] J. Gómez-Elvira, C. Armiens, L. Castañer, M. Domínguez, M. Genzer, F. Gómez, R. Haberle, et al., REMS: The environmental sensor suite for the Mars Science Laboratory Rover, Space Sci. Rev. 170 (2012) 583–640.
[23] J. Gómez-Elvira, C. Armiens, I. Carrasco, M. Genzer, F. Gómez, R. Haberle, V.E. Hamilton, et al., Curiosity's rover environmental monitoring station: Overview of the first 100 sols, J. Geophys. Res. 119 (2014) 1680–1688.
[24] T. Velasco, J.A. Rodríguez-Manfredi, The TWINS instrument on board mars insight mission, in: EGU General Assembly Conference Abstracts, vol. 17 of EGU General Assembly Conference Abstracts, Apr. 2015, pp. 2571.
[25] J. Pérez-Izquierdo, E. Sebastián, G.M. Martínez, A. Bravo, M. Ramos, J.A.R. Manfredi, The Thermal Infrared Sensor (TIRS) of the Mars Environmental Dynamics Analyzer (MEDA) instrument onboard Mars 2020, a general description and performance analysis, Measurement 122 (2018) 432–442.
[26] R. Giordano, A. Ianiro, T. Astarita, G.M. Carlomagno, Flow field and heat transfer on the base surface of a finite circular cylinder in crossflow, Appl. Thermal Eng. 49 (2012) 79–88. Thermal and Environmental Issues in Energy Systems (ASME/ATE/ UIT).
[27] S. Dhiman, J. Prasad, Inverse estimation of heat flux from a hollow cylinder in cross-flow of air, Appl. Therm. Eng. 113 (2017) 952–961.
[28] S. Soprani, A.J. Nørgaard, C. Nesgaard, K. Engelbrecht, Design and testing of a heat transfer sensor for well exploration tools, Appl. Therm. Eng. 141 (2018) 887–897.
[29] J. Merrison, H. Bechtold, H. Gunnlaugsson, A. Jesen, K. Kinch, P. Nornberg, K. Rasmussen, An environmental simulation wind tunnel for studying Aeolian transport on Mars, Space Sci. Rev. 56 (3–4) (2008) 426–437.
[30] D. Mueller, H. Abu-Mulaweh, Prediction of the temperature in a fin cooled by natural convection and radiation, Appl. Therm. Eng. 26 (2006) 1662–1668.
[31] J. Gomez-Elvira, Mars Science Laboratory Rover Environmental Monitoring Station RDR, pp. NASA Planetary Data System Data V1.0, MSL–M–REMS–6–ADR–V1.0, 2013.
[32] J. Gomez-Elvira, Mars Science Laboratory Rover Environmental Monitoring Station RDR,' pp. NASA Planetary Data System Data V1.0, MSL–M–REMS–4–ENVEDR–V1. 0, 2013.
[33] J. Gomez-Elvira, Mars Science Laboratory Rover Environmental Monitoring Station RDR, pp. NASA Planetary Data System Data V1.0, MSL–M–REMS–5–MODRDR–V1. 0, 2013.
[34] D.G. Murri, Simulation Framework for Rapid Entry, Descent, and Landing (EDL) Analysis, NASA Engineering and Safety Center Technical Assessment Report, vol. 1, no. NASA/TM-2010-216867, 2010.
[35] M. Schoenenberger, F.M. Cheatwoodt, P.N. Desai, Static Aerodynamics of the Mars Exploration Rover Entry Capsule, in: 43rd AIAA Aerospace Sciences Meeting and Exhibit, no. 0056, 2005.

[36] R.J. Kee, F.M. Rupley, J.A. Miller, M.E. Coltrin, J.F. Grcar, E. Meeks, H.K. Moffat, et al., CHEMKIN Collection. Reaction Design Inc, 3.6 ed., 2000.
[37] G.M. Martínez, C.N. Newman, A. De Vicente-Retortillo, et al., The modern near-surface martian climate: a review of in-situ meteorological data from viking to curiosity, Space Sci. Rev. 212 (1–2) (2017) 228–295.
[38] F. White, Viscous Fluid Flow, 2011.
[39] D. Viúdez-Moreiras, J. Gömez-Elvira, C.E. Newman, S. Navarro, M. Marin, J. Torres, M. de la Torre-Juárezthe MSL team, Gale surface wind characterization based on the Mars Science Laboratory REMS dataset. Part II: Wind probability distributions, Icarus 319 (2019) 645–656.
[40] P. Dey, A.K. Das, Numerical analysis of drag and lift reduction of square cylinder, Eng. Sci. Technol. Int J. 18 (4) (2015) 758–768.
[41] A. Okajima, Strouhal numbers of rectangular cylinders, J. Fluid Mech. 123 (1982) 379–398.
[42] S. Sanitjai, R.J. Goldstein, Forced convection heat transfer from a circular cylinder in crossflow to air and liquids, Int. J. Heat Mass Transf. 47 (22) (2004) 4795–4805.
[43] A. Kalendar, P.H. Oosthuizen, A numerical and experimental study of natural convective heat transfer from an inclined isothermal square cylinder with an exposed top surface, Heat Mass Transf. 49 (May 2013) 601–616.
[44] F. Sarvar, N.J. Poole, P.A. Witting, PCB glass-fibre laminates: Thermal conductivity measurements and their effect on simulation, J. Electron. Mater. 19 (12) (1990) 1345–1350.
[45] F. Incopera, D. Dewitt, T. Bergman, A. Lavine, Fundamentals of Heat and Mass Transfer, 6th ed., John Wiley and Sons, Inc., 2007.
[46] A. Okajima, Numerical simulation of the flow around rectangular cylinders, J. Wind Eng. Ind. Aerod. 33 (1–2) (1990) 171–180.
[47] J. Ortega-Casanova, On the onset of vortex shedding from 2D confined rectangular cylinders having different aspect ratios: Application to promote mixing fluids, Chem. Eng. Process 120 (2017) 81–92.